Dystrophin deficiency impairs cell junction formation during embryonic myogenesis

Elise Mozin[1], Emmanuelle Massouridès[2], Virginie Mournetas[3], Clémence Lièvre[1], Audrey Bourdon[1], Dana L Jackson[4], Jonathan S Packer[4], Cole Trapnell[4], Caroline Le Guiner[1], Oumeya Adjali[1], Christian Pinset[2], David L Mack[5] and Jean-Baptiste Dupont[1,*]

Affiliations:

1: Nantes Université, CHU Nantes, INSERM, TARGET, F-44000 Nantes, France

2: Centre d'Etude des Cellules Souches, I-Stem, AFM, F-91100 Corbeil-Essonnes, France

3: ADLIN Science, F-91058 Evry, France

4: Department of Genome Sciences, University of Washington School of Medicine, Seattle, WA 98105, USA

5: Institute for Stem Cell and Regenerative Medicine, Department of Rehabilitation Medicine, University of Washington, Seattle, WA 98109, USA

Contact info: *Correspondence: jean-baptiste.dupont@univ-nantes.fr; Twitter: @dpt_jb

Summary

Mutations in the *DMD* gene lead to Duchenne muscular dystrophy, a severe X-linked neuromuscular disorder which manifests itself as young boys acquire motor functions. DMD is diagnosed after 2 to 4 years, but the absence of dystrophin has an impact before symptoms appear in patients, which poses a serious challenge in the optimization of standards of care. In this report, we investigated the early consequences of dystrophin deficiency during skeletal muscle development. We used single-cell transcriptome profiling to characterize the myogenic trajectory of human pluripotent stem cells and showed that DMD cells bifurcate to an alternative branch when they reach the somite stage. Here, dystrophin deficiency was linked to marked dysregulations of cell junction families involved in the cell state transitions characteristic of somitogenesis. Altogether, this work demonstrates that *in vitro*, dystrophin deficiency has early consequences during myogenic development, which should be considered in future therapeutic strategies for DMD.

Keywords: Duchenne muscular dystrophy, DMD, myogenesis, cell junctions, somite, hiPSCs

Introduction

Mutations in genes involved in skeletal muscle functions trigger a spectrum of diseases which can lead to significant motor and respiratory impairments, sometimes shortly after birth[1–3]. The cellular and molecular mechanisms of these diseases are complex and result in the breakdown of skeletal muscle homeostasis. In Duchenne muscular dystrophy (DMD) patients, the lack of functional dystrophin causes systemic pathological perturbations, which mostly affect striated muscles and the central nervous system. In muscle cells, *DMD* mutations lead to plasma membrane fragility, calcium overload, oxidative stress, mitochondrial impairments and the development of an inflammatory environment and of a fibro-adipogenic process[4]. As muscles develop in the absence of dystrophin, capturing the pathological molecular cascade downstream of the mutation and tracking progression over time are difficult using animal models. Early studies described prenatal signs of muscle wasting in presymptomatic *mdx* mice and GRMD puppies[5,6]. Signs of muscle damage such as variable myotube diameter, hyaline fibers and internal nuclei had also been observed in fetuses at risk for DMD[7,8]. The most well-characterized functions of dystrophin have been described in fully differentiated skeletal muscle cells, which express the longest isoform of the protein (Dp427m) to connect the contractile machinery with the sarcolemma through the dystrophin-associated protein complex (DAPC)[4]. However, the expression of the *DMD* locus gives rise to multiple other isoforms, and its regulation during development is controlled by complex mechanisms. In the embryo, skeletal muscles emerge from the paraxial mesoderm, which differentiates into transient metameric structures called somites, and then into the dermomyotome[9]. This involves a succession of well-orchestrated cell division, migration and transitions between epithelial and mesenchymal states, that later give rise to myogenic progenitors with migratory properties[10–12]. In this context, the expression of dystrophin and the consequences of pathological mutations during skeletal muscle development remain to be characterized in a reliable model.

Pluripotent stem cells represent a proxy for human embryonic development, and they allow the characterization of early disease mechanisms in a dish[13,14]. Several groups have published protocols to differentiate human induced pluripotent stem cells (hiPSCs) into paraxial mesoderm progenitors, somite intermediates, dermomyotome and ultimately skeletal muscle progenitors[15–18]. Recently, our group has used hiPSCs from DMD patients to demonstrate that marked transcriptome dysregulations occur prior to skeletal muscle commitment[19]. Characterization of the *DMD* gene expression during early mesoderm

induction had led to the identification of an embryonic isoform of dystrophin (Dp412e) in mesoderm progenitors and embryoid bodies[20]. This isoform possesses an alternative exon 1 and encodes an N-truncated protein starting in exon 6 of the skeletal muscle dystrophin isoform (Dp427m). However, its functions and molecular partners have remained unknown so far.

Transcriptomic analysis of hiPSCs and their derivatives at single-cell resolution offers the unprecedented opportunity to shed light on complex biological processes such as embryonic development and to investigate the consequences of disease-causing mutations in any given lineage intermediate. In particular, single-cell RNA-sequencing (scRNA-Seq) have helped characterize the diversity of skeletal muscle cells involved in muscle development[21,22], specification[23,24], ageing[25–27], and in various models of DMD[28–31]. Reconstruction of single-cell trajectories thanks to pseudotemporal ordering of cells have been used to describe differentiation dynamics of myoblasts and the gene expression profiles associated with various differentiation outcomes[32,33]. Studying the divergence of this trajectory when hiPSCs harbor a mutated *DMD* will provide a deeper understanding of the molecular drivers of pathology and the cascade of compensatory perturbations downstream of the mutation.

In this study, we established the single-cell trajectory of healthy and dystrophin-deficient hiPSCs subjected to myogenic differentiation. We showed that hiPSCs derived from a DMD patient diverged from healthy control cells as early as the somite stage (differentiation Day 10), and that the differences propagated as differentiation progressed. By focusing on Day 10 and including an isogenic DMD line engineered from the healthy control by CRISPR-Cas9, we demonstrated that several cell junction gene families were markedly dysregulated as a consequence of dystrophin deficiency. Further characterization of the somite progenitors derived from hiPSCs identified epithelial and mesenchymal populations coexisting *in vitro*, reflecting the cell state transitions occurring in the embryo, and that the formation of epithelial islets is altered in the absence of dystrophin. Finally, we confirmed our results in three additional DMD hiPSC lines by immunostaining and analysis of previous bulk RNA-Seq data generated in our group, which strongly suggests that *DMD* mutations have significant consequences during prenatal development, in relation to the dynamics of cell junctions during somitogenesis.

Results

DMD hiPSCs bifurcate to an alternative branch of the myogenic trajectory

Human iPSCs from a DMD patient harboring an exon 50 deletion in the *DMD* gene were subjected to directed differentiation into the skeletal muscle lineage in parallel with a healthy control[34], using a transgene-free and serum-free protocol[15]. Microscopic monitoring showed extensive cell proliferation and densification into multilayered cultures over time (Figure S1A). The differentiation was stopped at Day 28 when fields of thin and spindly cells resembling myotubes could be observed in the healthy control line. To investigate the dynamics of myogenic differentiation and the impact of dystrophin deficiency, cells were isolated at ten successive differentiation time points from Day 0 (D0) to Day 28 (D28), tagged with barcoded primers during *in situ* reverse-transcription and pooled for single-cell combinatorial indexing RNA-Seq (sci-RNA-Seq, Figure 1A)[35]. A total of 1917 individual cells could be retrieved from 20 distinct samples corresponding to the 2 hiPSC lines across 10 time points (Table S1), and used in the subsequent clustering analyses. After Uniform Manifold Approximation and Projection (UMAP) for dimension reduction, cells were distributed among 7 clusters expressing well-defined marker genes associated with pluripotency at Day 0 (*e.g. POU5F1*, clusters 4-5), primitive streak at Day 2 (*T,* cluster 5), paraxial mesoderm at Day 2-4 (*TBX6*, cluster 3), somite and dermomyotome at Day 7-10 (*PAX3*, clusters 2-7), and ultimately skeletal muscle progenitor cells from Day 22-28 (*PAX7*, *MYOD1*, cluster 1) (Figure S1B-C). Interestingly, DMD and healthy control cells were intermingled into superimposed clusters during the first week (Day 0 – 7), but from Day 10, they started to form distinct cell populations (Figure 1B-C). Single-cell trajectory reconstruction with Monocle[33] identified a branching point between Day 7 and Day 10, from which most of the cells segregated on two distinct branches in a genotype-dependent manner (Figure 1D-E). More precisely, 86 % of the healthy cells post branching point were on a single branch, while 86 % of the DMD cells were on the other branch (Figure S1D). Branch expression analysis modelling (BEAM) identified thousands of differentially-expressed genes (DEG) along the WT and the DMD-enriched branches. The most significant candidates (1987 genes with p-adj < 0.0001) were clustered based on their expression dynamics on the two branches for gene ontology analysis (Figure 1F, Table S2). Interestingly, modules of genes overexpressed along the Healthy branch were enriched in terms related to muscle development (*e.g.* Muscle cell differentiation, Muscle contraction, Actin cytoskeleton organization). In contrast, gene modules overexpressed along the

DMD branch matched with GO terms related to the development of alternative lineages, particularly neurons (*e.g.* Neurogenesis, Synapse organization, Axon guidance). To gain insight into the regulation of myogenesis in pseudotime, differential expression of paraxial mesoderm, somite and skeletal muscle markers was assessed between the two branches. Significant differences in pseudotemporal dynamics and expression were found for critical regulators of myogenesis, including *MYOD1*, *MYOG*, *MEF2C*. Notably, the master regulators *MYOD1* and *MYOG* were almost unexpressed in DMD cells, in contrast with *PAX7* and *MEF2C*, although for the latter, expression in DMD cells was significantly reduced as pseudotime progressed (Figure 1G). In addition, genes coding for important structural proteins such as *MYH3*, *MYH8*, *DES* or *TTN* were also found significantly dysregulated (Figure 1G). Thus, hiPSCs derived from a DMD patient deviated from the myogenic trajectory followed by healthy control cells.

DMD cells exhibit a marked dysregulation of cell junction genes at Day 10

We focused our analysis at Day 10, the time point at which the deviation of DMD cells was first evident on the single-cell trajectory. We observed that the sci-RNA-Seq data subset corresponding to the "Day 10" time point formed a single UMAP cluster with a clear separation between DMD cells and healthy controls (Figure 2A). Differential expression analysis using the regression model from Monocle 3 identified 94 genes significantly dysregulated in DMD cells (adjusted p-value < 0.01) (Table S3). Among these differentially expressed genes (DEGs), we notably found multiple cell junction and extracellular matrix genes, such as cadherins and proto-cadherins (*CDH11*, *PCDH9*), integrins (*ITGA1*, *ITGA4*, *ITGB1*, *ITGAV*), fibronectin (*FN1*) and numerous collagens (*COL1A2*, *COL3A1*, *COL4A1*, *etc.*). Gene ontology (GO) analysis confirmed significant enrichments in related biological processes, such as cell-matrix interaction (p = 5.6E-4), cell-cell adhesion (p = 6.9E-7), extracellular matrix organization (p = 6.9E-4) and cell junction organization (p = 4.0E-2) (Figure 2B). PANTHER Pathway enrichment analysis showed that the DEGs were particularly enriched in genes involved in the integrin and cadherin signaling pathways (p = 2.4E-12 and p = 4.2E-2, respectively) (Figure 2C). Of note, the GO analysis also indicated that DEGs included regulators of key developmental processes in non-muscle lineages, such as neurogenesis and axon guidance (*SEMA3A*, *EPHA3*, *NRP1*, *NEFL*, *UNC5C*), and angiogenesis (*ANGPT1*, *THSD7A*). Neuronal by-products have already been observed when hiPSCs are differentiated with the protocol used in this first analysis[36].

In our study, the DMD hiPSC line might be more prone to such uncontrolled differentiation events, leading to the formation of more alternative cell types.

Next, we assessed the robustness of our results using a distinct myogenic differentiation protocol. We selected a commercial media formulation previously shown by our group and others to generate a homogeneous muscle cell population[16,19]. hiPSCs were differentiated up to Day 10 with this new protocol and analyzed by single-cell RNA-Seq. In addition to the DMD patient hiPSC line, we included an isogenic DMD CRISPR line engineered from the healthy control line by deleting the entire exon 45 of the *DMD* gene together with 17 base pairs in exon 54[37], leading to an absence of dystrophin protein at any differentiation stage from hiPSCs to myotubes (Figure S2A). At Day 10, we confirmed that cells express somite marker genes, and we showed that the DMD patient line expressed significantly higher levels of *PAX3*, *MEOX1* and *NR2F1* than the healthy control, and lower levels of *MET*, *PTN* and *NR2F2* (Figure 2D). Interestingly, the CRISPR line presented with a less pronounced dysregulation profile, yet statistically significant for all the above-mentioned marker genes except *NR2F1*. After dimensional reduction, the UMAP plot revealed that DMD cells and healthy controls were separated into distant clusters. The CRISPR clusters were found in between, closer to the DMD cells with only a small fraction overlapping with healthy cells (Figure 2E). We then conducted differential expression analysis using the Monocle 3 pipeline. DMD and CRISPR cells showed 4,565 and 2,913 differentially expressed genes respectively when compared to the healthy control line (p-adj < 0.01, Table S4). Among these, 1,885 genes were differentially expressed in both lines, which represents the core gene set dysregulated at the somite stage as a direct consequence of the DMD mutation (Figure 2F). Of note, this result also illustrated the influence of the genetic background on disease manifestation at the transcriptome level, as 36 % of the CRISPR-induced dysregulations were not present in the unrelated DMD patient line. Importantly however, the common DEGs also included 55 of the 94 genes (59 %) found significantly dysregulated at Day 10 with the initial protocol, highlighting the overlap between the two single-cell RNA-Seq data sets. To go further, we performed GO analysis on the 1,885 overlap genes, and observed an enrichment in terms related to cell junctions, such as desmosome organization (p = 7.2E-3), tight junction organization (p = 4.4E-4), and cell junction assembly (p = 2.2E-11) (Figure 2G). Finally, we analyzed the detailed expression of key cell-cell junction gene families, and we observed that tight junction genes such as claudins (*CLDN*), ocludin (*OCLN*) and tight junction proteins (*TJP*), but also

166 desmosome genes such as desmoplakin (*DSP*), desmogleins (*DSG*) and desmocollins (*DSC*) were
167 markedly down-regulated in the DMD line. In contrast, multiple genes from the protocadherin (*PCDH*) and
168 cadherin (*CDH*) families were up-regulated (Figure 2H). Similar to our previous observations, the CRISPR
169 line showed an intermediary dysregulation profile for all cell junction protein families (Figure 2I). In the
170 previous sci-RNA-Seq data analysis, adherens junctions were also found particularly affected in the BEAM
171 gene list, including members of the *CDH* and *PCDH* families, together with genes encoding catenins
172 (*CTNN*) (Figure S2B). Altogether, our results suggest a major role for cell junction gene families in the
173 initiation and progression of DMD during development.

174 **Dystrophin deficiency does not compromise myotube formation despite impaired upstream cell**
175 **state transitions**

176 In spite of earlier reports suggesting the existence of prenatal disease manifestations at the cellular
177 and molecular levels, DMD patients are born with functional muscles. We assessed the ability of DMD and
178 CRISPR hiPSCs to differentiate into multinucleated myotubes. Somite progenitors were amplified,
179 passaged in a Myoblast medium and further differentiated with a Myotube Fusion medium[16]. At Day 25,
180 cells were stained for two skeletal muscle proteins: myosin heavy chains and α-actinin. Multinucleated
181 myotubes with striation patterns could be observed in the 3 hiPSC lines (Figure 3A). We quantified the area
182 positive for α-actinin and obtained comparable fluorescent signals in the 3 hiPSC lines representing 34 %
183 of the total area on average (Figure 3B). Thus, the early dysregulations of the transcriptome observed at
184 the somite stage do not impact myotube formation *in vitro*. Prior to terminal differentiation, hiPSCs undergo
185 several rounds of amplification and passages as they transition through the successive developmental
186 intermediates. These culture conditions may introduce positive bias by retaining only the cells most capable
187 of differentiation, hereby masking prior developmental deficiency. Hence, we examined the appearance of
188 cell cultures at the somite stage, around Day 7 to Day 10. During paraxial mesoderm and somite
189 development in the embryo, progenitors undergo successive epithelial-mesenchymal and mesenchymal-
190 epithelial transitions, accompanied by a well-coordinated remodeling of the cell-cell and cell-matrix
191 junctions[10–12,38]. In our cell cultures at Day 10, we observed two cell populations with distinct features: (1)
192 spindly, refringent, tightly packed cells with a mesenchymal morphology and (2) larger, more flattened cells

in close contact to one another similar to squamous or cuboidal epithelia (Figure 3C). These larger cells were first detected at Day 8 and progressively form "epithelial" islets surrounded by a "mesenchymal" environment until Day 10 (Figure S3). We performed immunofluorescence targeting E-cadherin (E-cad), a cell junction protein characteristic of epithelial cells and Vimentin (Vim), a cytoskeleton protein expressed mostly in mesenchymal cells. As anticipated, the islets expressed high levels of E-Cad and were negative for Vim, and the cells in between expressed Vim but no E-cad (Figure 3D). The fluorescent signal was quantified in the 3 hiPSC lines at Day 10 and we found ~10% E-cad-positive cells in both the Healthy control line and the CRISPR line, and less than 1% in the DMD line (Figure 3E). We next assessed the expression of C-Met, a receptor tyrosine kinase expressed at the membrane of epithelial cells during dermomyotome development from the somites and critical for subsequent myoblast migration[39]. Interestingly, we observed a strong C-Met expression in epithelial islets, suggesting a dermomyotome identity, but no C-Met-positive cell was found in the DMD line. Interestingly, differentiation of the CRISPR line resulted in C-Met expression at Day 10, but at a level 5 times lower than in the healthy control (p-val = 0.029) (Figure 3F-G). This suggests that somitogenesis and the associated cell state transitions are altered in the absence of dystrophin, but that additional factors have an influence, depending on the genetic background.

Somitogenesis and cell junction genes are dysregulated in three additional DMD hiPSC lines

In order to increase the power of our study and extend it to additional DMD backgrounds, we compared our findings with an RNA-Seq dataset previously generated in our group to describe the myogenic differentiation of DMD hiPSCs at defined time points (https://muscle-dmd.omics.ovh/)[19]. More precisely, hiPSC lines from three independent DMD patients and three healthy individuals were differentiated in triplicates with a commercial media formulation[16] and cells were collected for bulk RNA-Seq at several time points (Figure S4). Interestingly, the transcriptome of DMD hiPSCs was shown to markedly diverge from healthy controls at Day 10, when somite marker genes are expressed[19]. Immunostaining at Day 10 showed the presence of epithelial islets expressing C-Met in the 6 hiPSC lines, but at a level 4.7 lower in the 3 DMD patient lines (p = 0.0003), confirming our previous observation (Figure 4A-B). We analyzed the RNA-Seq data set and identified 1450 genes significantly dysregulated at Day 10 in the DMD cell lines (abs(log2 fold-change) ≥ 1 and adjusted p-value ≤ 0.01, Figure 4C, Table S5).

Importantly, GO analysis indicated a significant enrichment in genes involved in the formation of cell junctions (Figure 4D), which confirms their importance in the initial manifestation of DMD during somite differentiation. Particularly, desmosome organization (GO:0002934) was affected in DMD cells, with a significant downregulation of *GRHL1* (log FC = -2.5, p-val = 3.7E-06), *JUP*, (log FC = -1.0, p-val = 7.7E-04), *PERP* (log FC = -1.4, p-val = 1.2E-08), *PKP2* (log FC = -1.5, p-val = 2.6E-03) and *PKP3* (log FC = -2.9, p-val = 1.1E-03) (Figure 4E). Tight junction organization (GO:0120193) was also perturbed by the absence of dystrophin, with dysregulation of gene members of the claudin (CLDN), cadherin (CDH) and protocadherin (PCDH) families (Figure 4E). Similar to our previous findings, we noticed that most gene families were downregulated in DMD cells, with the exception of the protocadherin (*PCDH*) family, in which 8/9 genes were upregulated (*PCDH17*, *PCDHA2*, *PCDHA7*, *PCDHB18P*, *PCDHGA3*, *PCDHGA4*, *PCDHGA5*, *PCDHGB3*, mean log FC = 1.5) and only 1 was downregulated (*PCDHA13*, log FC = -1.7).

Altogether, our study combines sequencing and imaging data from four unrelated DMD patient hiPSC lines and four healthy controls plus one isogenic DMD mutant, and indicates that dystrophin deficiency leads to major dysregulations of cell junction gene families participating in cell state transitions during somite development.

Discussion

Thanks to carefully defined differentiation protocols, hiPSCs and their derivatives can help better understand human embryonic development and investigate the early impact of mutations leading to specific genetic disorders without the use of embryos[13]. Using a published protocol recapitulating key developmental steps of human myogenesis, we provide here a temporally resolved dataset spanning ten time points along the differentiation of healthy and DMD hiPSCs from pluripotency to the skeletal muscle lineage. We observed that cells first go through intensive transcriptional changes as they leave pluripotency and adopt an early mesodermal fate. After Day 7, they stabilize as they become somite progenitors and their progenies (*i.e.* dermomyotome and skeletal muscle cells). The developmental trajectory computed from our pseudotime data showed that fractions of cells reach the end of the myogenic process as early as Day 10, reflecting the fact that cells differentiate in a heterogeneous and asynchronous manner[32,40,41].

During the second half of the differentiation process, cells that are "behind schedule" probably "catch up" or remain stalled on an abortive developmental path. At the differentiation end stage, we observed that a majority of cells did not express canonical myogenic markers such as *MYOD1*, *MYOG* or *PAX7*. However, most of them were positive for the myocyte-specific enhancer factor 2C (*MEF2C*), known to be involved in myogenesis but also in the development of a myriad of other tissues (*i.e.* heart, nervous system, vasculature, bone and cartilage)[42]. Neural cells have already been identified as cellular by-products generated alongside muscle cells with the myogenic differentiation protocol used in the first part of this study[36]. For this reason, a commercial myogenic media known to produce more homogeneous cell populations at the successive developmental steps was also used in this study[16,19,43]. This allowed us to confirm that similar to what is seen in DMD patients, the absence of dystrophin does not compromise the ability of hiPSCs to differentiate into myotubes. However, it may delay differentiation and / or deflect a fraction of cells from the skeletal muscle into alternative or abortive lineages during embryogenesis, which might go unnoticed *in vitro* due to the amplification and passage steps that are part of the differentiation protocols.

Here, we discovered that dystrophin mutation leads to the dysregulation of cell junctions during the successive cell state transitions which come with the *in vitro* differentiation of "somite-like" cell monolayers.

Somites are transient metameric structures emerging from the paraxial mesoderm in the embryo. They give rise to multiple tissues such as the axial dermis, cartilages, bones and skeletal muscles of the axis and limbs[44,45]. Individual somites are patterned along the dorsal-ventral axis into the sclerotome at the ventral pole and the dermomyotome at the dorsal pole. Myogenic progenitors delaminate from the dermomyotome to form primary multinucleated myofibers[12,46,47]. These developmental steps involve coordinated gene expression and successive transitions between a mesenchymal and an epithelial state[10–12]. We showed that the hiPSC model recapitulates key features of somitogenesis when subjected to myogenic differentiation, both at the level of their morphology and gene expression program. As a monolayer, somite progenitors derived from control hiPSCs spontaneously organize into discrete "epithelial islets", surrounded by mesenchymal cells. In the embryo, somite epithelialization requires the activity of *Paraxis* and the somites of *Paraxis-/-* murine embryos showed dysregulated somitogenesis and disorganized cell

junctions[11,48]. The activity of the Rho family small GTPases Cdc42 and Rac1 also plays an essential role in the epithelialization during somitogenesis[49], possibly by controlling the architecture of the cytoskeleton and the remodeling of cell junctions during the successive cell state transitions. One appealing hypothesis would be that during somite development, the embryonic isoform of dystrophin serves as a stabilizing anchor in newly formed epithelial cells. Testing this hypothesis will require further investigations in appropriate model systems, as Dp412e is specific to a subgroup of anthropoids, including humans.

Multiple protein isoforms have been described from the *DMD* locus, each with a defined expression pattern[50–52], but their function remains to be precisely characterized. In skeletal and cardiac muscles, the Dp427m dystrophin isoform is known to interact with the dystrophin-associated protein complex (DAPC), but in other tissues, the protein partners of other isoforms are less characterized. Recent studies have described association of dystrophin with alternative partners in specific cells and tissues, such as aquaporin 4, calcium and potassium channels[53–57]. However, the exact molecular mechanisms driven by these interactions reman to be investigated. Dp412e was identified as an “embryonic” isoform induced during the formation of early mesoderm progenitors and embryoid bodies from hiPSCs[20]. Here, our results strongly suggest that Dp412e has specific roles during embryonic development and the cell transitions occurring when somites develop, which remain to be precisely determined.

Altogether, our study leads us to consider DMD even more as a developmental disease, even though patients are born without apparent symptoms. A better understanding of the “invisible” DMD initiation events during development and early postnatal life will help identify biomarkers early in the course of disease progression, which in turn could accelerate diagnosis and pinpoint new therapeutic targets.

Acknowledgments

This work was funded by the INSERM ATIP Avenir program, Nantes Université, the University Hospital of Nantes, the Association Française contre les Myopathies (AFM) Téléthon, Genopole, and by the Wellstone Muscular Dystrophy Cooperative Research Center supported by the National Institute of Health (NIH, grant number U54 AR065139). We thank the GenoA Genomics Core Facility and the BiRD Bioinformatics Core Facility (Nantes Université, SFR Bonamy, UMS Biocore, Biogenouest), which is part of the Institut Français de Bioinformatique (ANR-11-INBS-0013) for the access to the computing and storage infrastructure and their help with sequencing and processing the single-cell libraries. We acknowledge the IBISA MicroPICell facility (Nantes Université, SFR Bonamy, UMS Biocore, Biogenouest), member of the national infrastructure France-Bioimaging supported by the French national research agency (ANR-10-INBS-04).

Author contributions

Conceptualization: CP, DLM, JBD; Methodology: EMo, CL, JBD; Software: VM, JSP, CT, JBD; Validation: EMo, CL, JBD; Formal analysis: EMo, CL, JBD; Investigation: EMo, EMa, VM, CL, AB, DLJ, JBD; Resources: AB, CT, OA, CP, DLM, JBD; Data Curation: EMo, VM, JSP, JBD; Writing – Original Draft: EMo, CL, JBD; Writing – Review & Editing: EMo, EMa, VM, CL, CT, CLG, OA, CP, DLM, JBD; Visualization: EMo, CL, JBD; Supervision: CT, CLG, OA, CP, DLM, JBD; Project administration: JBD; Funding acquisition: EMa, VM, OA, CP, DLM, JBD.

Declaration of interests

The authors declare no competing interests

Inclusion and diversity

Our research group supports inclusive, diverse and equitable conduct of research.

Figures & Figure Legends

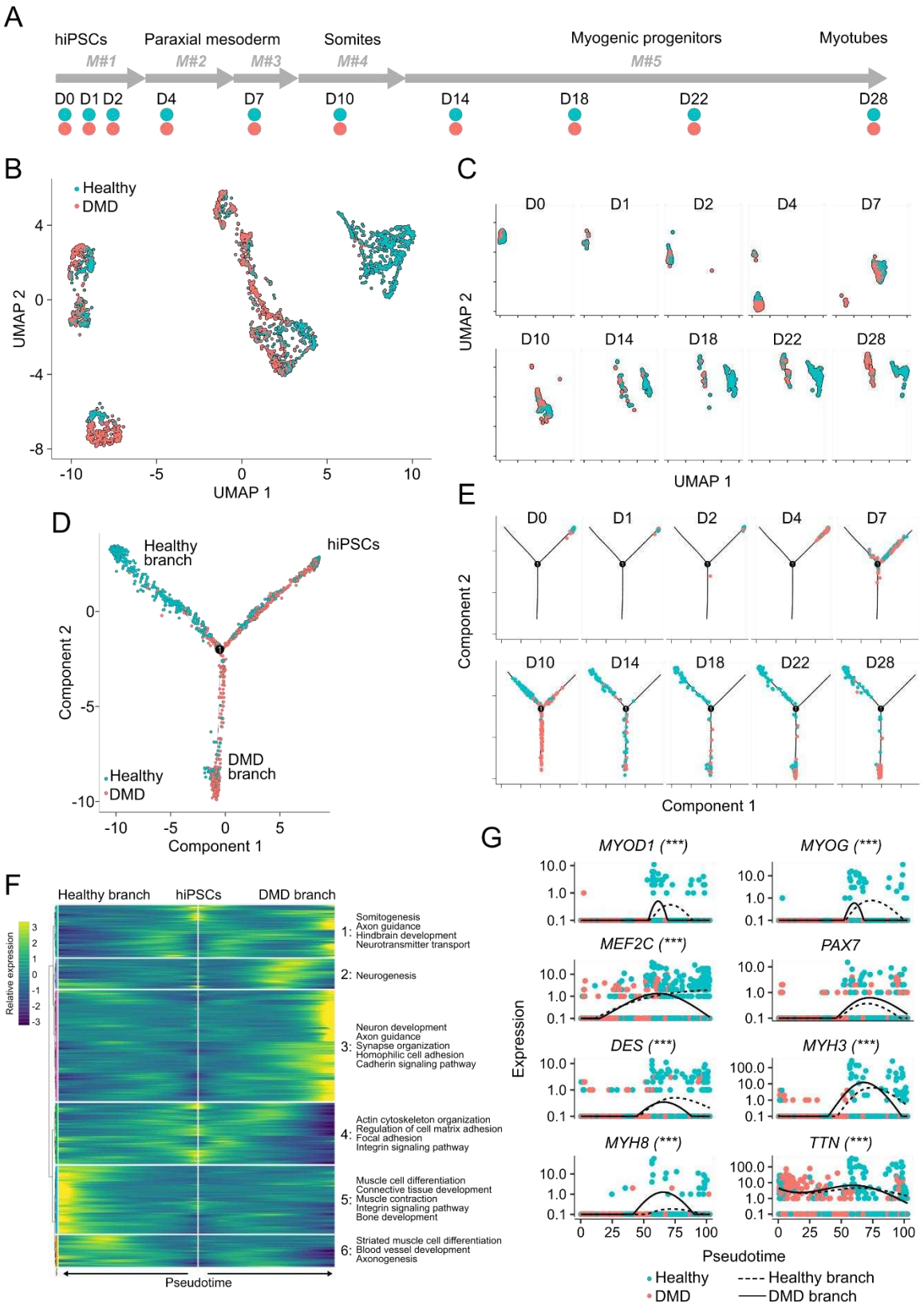

316 **Figure 1:** Myogenic differentiation of DMD and healthy control hiPSCs at the single-cell resolution. (A) Cell
317 collection timeline along hiPSC myogenic differentiation using the combination of 5 defined media (M#1 to
318 M#5) described previously[15]. D0 to D28: Day 0 to Day 28. (B) UMAP plot showing the 1917 individual cells
319 colored by hiPSC line of origin. (C) Deconvolution of the UMAP plot by collection time point (D0 to D28).
320 (D) Single-cell trajectory capturing the dynamics of myogenic differentiation as DMD and Healthy hiPSCs
321 progress along the initial common branch (hiPSCs) to the bifurcation point (1) and one of the two alternative
322 branches. (E) Deconvolution of the single-cell trajectory by collection time point (D0 to D28). (F) Branched
323 expression analysis modeling identifying modules of genes with branch-dependent expression. Key Gene
324 Ontology terms associated with each individual module are indicated on the right-hand side. (G) Gene
325 expression kinetic in pseudotime for myogenic markers along the Healthy (dotted line) and the DMD (full
326 line) branch. Each dot shows an individual cell with its computed pseudotime value. Significant differences
327 in branch-dependent expression are indicated with *** (p-adj < 0.001).

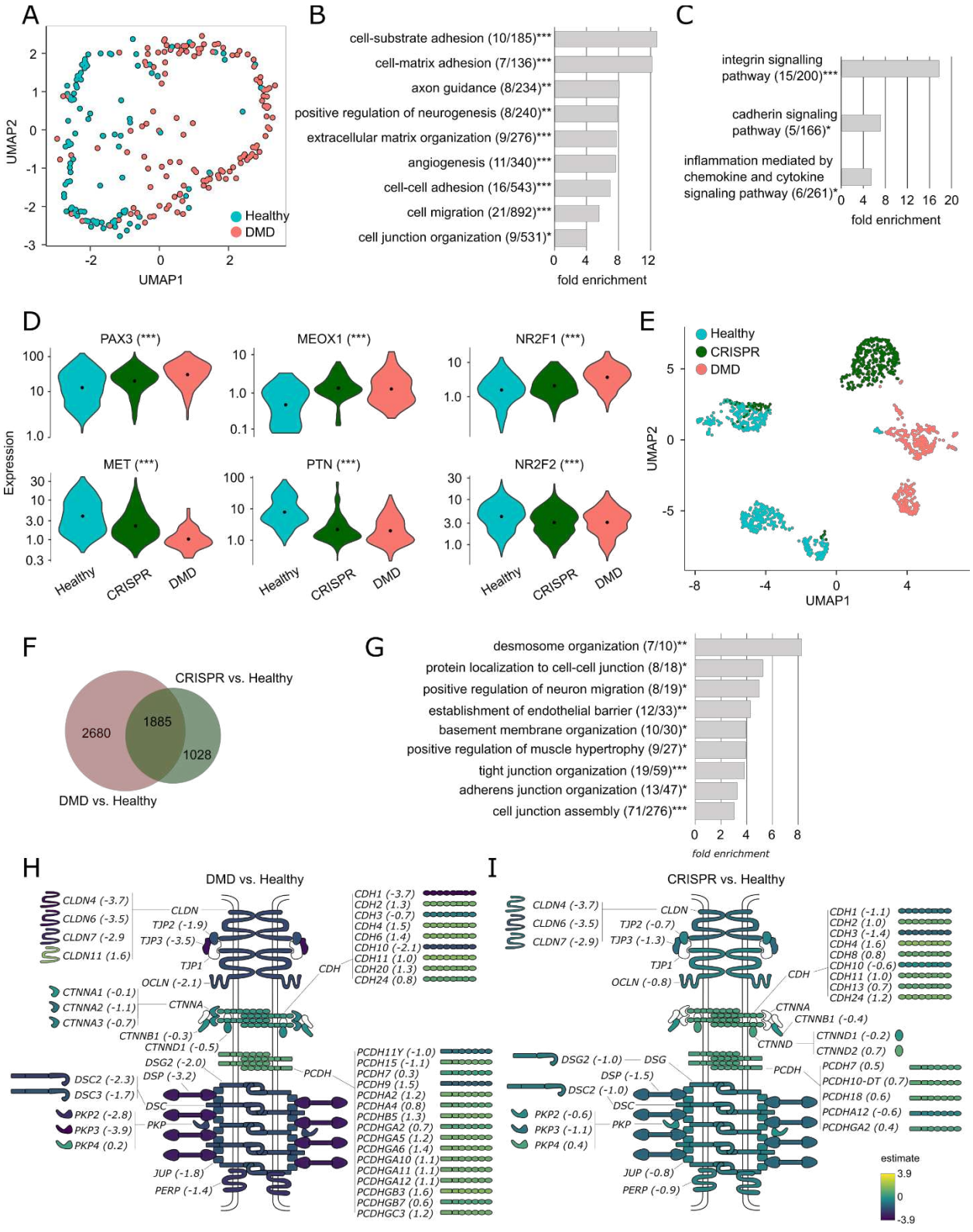

328

329

Figure 2: DMD cells exhibit a marked dysregulation of cell junction genes at Day 10. (A) UMAP plot of the individual cells collected at Day 10 from the sci-RNA-Seq data set (Figure 1) colored by their hiPSC line of origin. (B-C) Gene Ontology (B) and Pathway enrichment (C) analyses performed with the 94 genes differentially expressed in DMD cells at Day 10 in the sci-RNA-Seq data set. (D) Violin plots showing the expression of somite marker genes in single cells from Healthy, CRISPR and DMD hiPSCs at Day 10. (E) UMAP plot showing the 3566 individual cells colored by their hiPSC line of origin. (F) Venn diagram of the differentially expressed genes in DMD and CRISPR hiPSC lines at Day 10. The absolute numbers of genes are indicated in the appropriate sections. (G) Gene ontology analysis with the 1885 genes differentially expressed in both the DMD and the CRISPR hiPSC lines at Day 10, showing a selection of significantly enriched biological processes. Legend: * false discovery rate (FDR) < 0.05; ** FDR < 0.01; *** FDR < 0.001; (X/Y): number of genes from the GO category found differentially expressed in the dataset / total number of genes in the GO category. (H-I) Differential expression of cell junction genes and potential implications at the protein level in the DMD (H) and CRISPR (I) hiPSC lines. Fold change estimates from single-cell data are indicated between brackets and color-coded for each protein. CLDN: claudin; OCLN: occludin; TJP: tight junction protein; CDH: cadherin; CTNN: contactin; PCDH: protocadherin; DSG: desmoglein; DSP: desmoplakin; DSC: desmocollin; PKP: plakophilin; JUP: plakoglobin; PERP: p53 apoptosis effector related to PMP22.

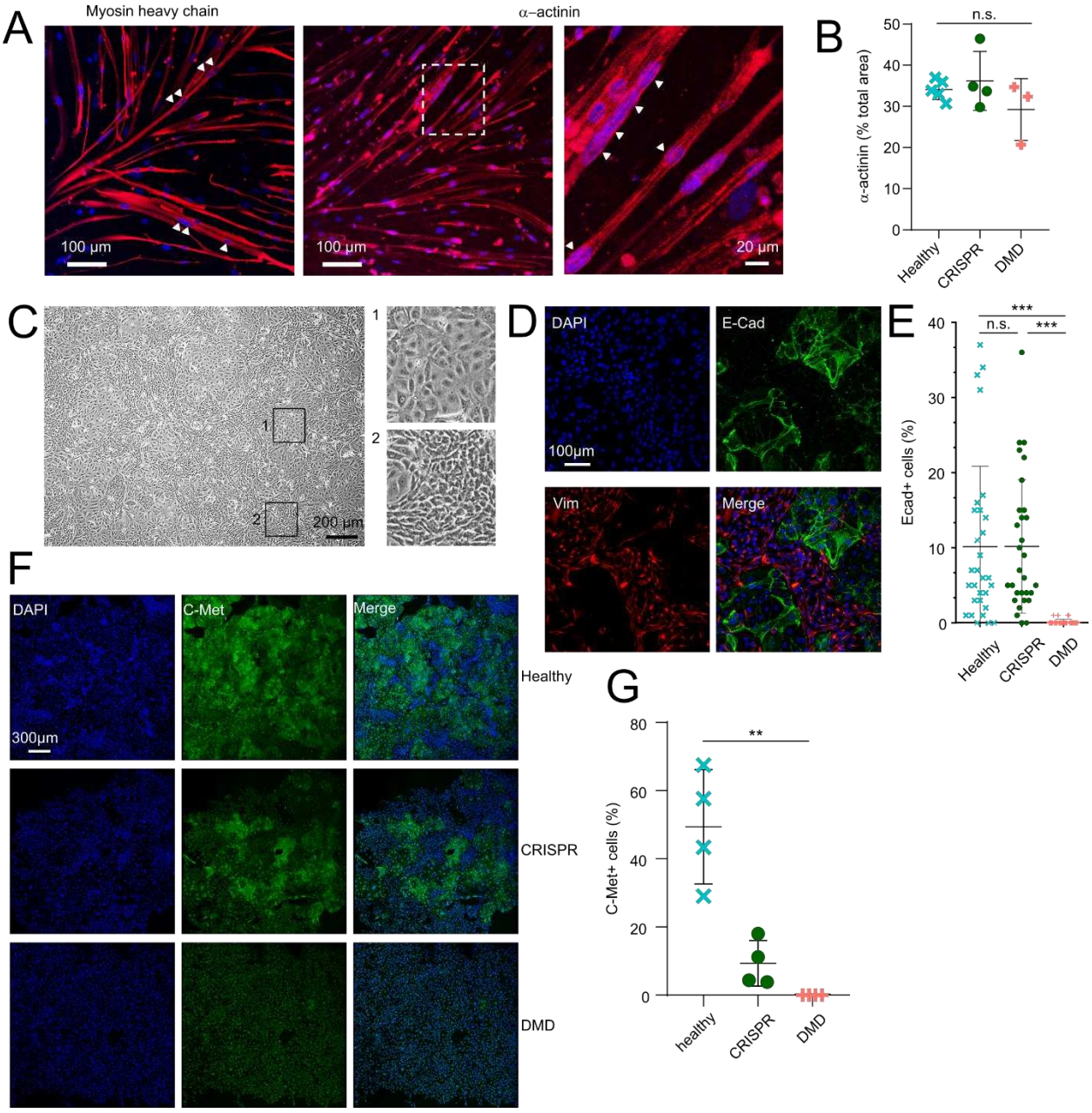

Figure 3: DMD does not compromise myotube formation despite altered upstream cell state transitions. (A) Fluorescent staining of myosin heavy chains and a-actinin (red) in myotubes derived from Healthy hiPSCs. Arrowheads indicate multinucleation and the right panel focuses on a striation pattern. (B) Quantification of the a-actinin fluorescent area in the three cell lines, expressed as a percentage of total area (n = 3 to 5 panels by cell line). (C) Optical microscopy with phase contrast of somite progenitors derived from hiPSCs. Insets 1 and 2 highlight the “epithelial-like” and “mesenchymal-like” cell populations. Scale bar = 200µm. (D) Detection of E-Cad and Vim in somite progenitors derived from hiPSCs by

355 immunofluorescence and confocal microscopy. (E) Quantification of the percentage of E-Cad-positive cells
356 in the Healthy, DMD and CRISPR hiPSC lines at Day 10 in three replicate experiments (N = 10 panels by
357 experiment). n.s. not significant; *** p-value < 0.001. (F) Detection of C-Met in the three hiPSC lines by
358 immunostaining and confocal microscopy at differentiation Day 10. (G) Quantification of the C-Met
359 fluorescent area normalized by the number of nuclei. Imaging was performed on four large mosaic panels
360 per cell line.

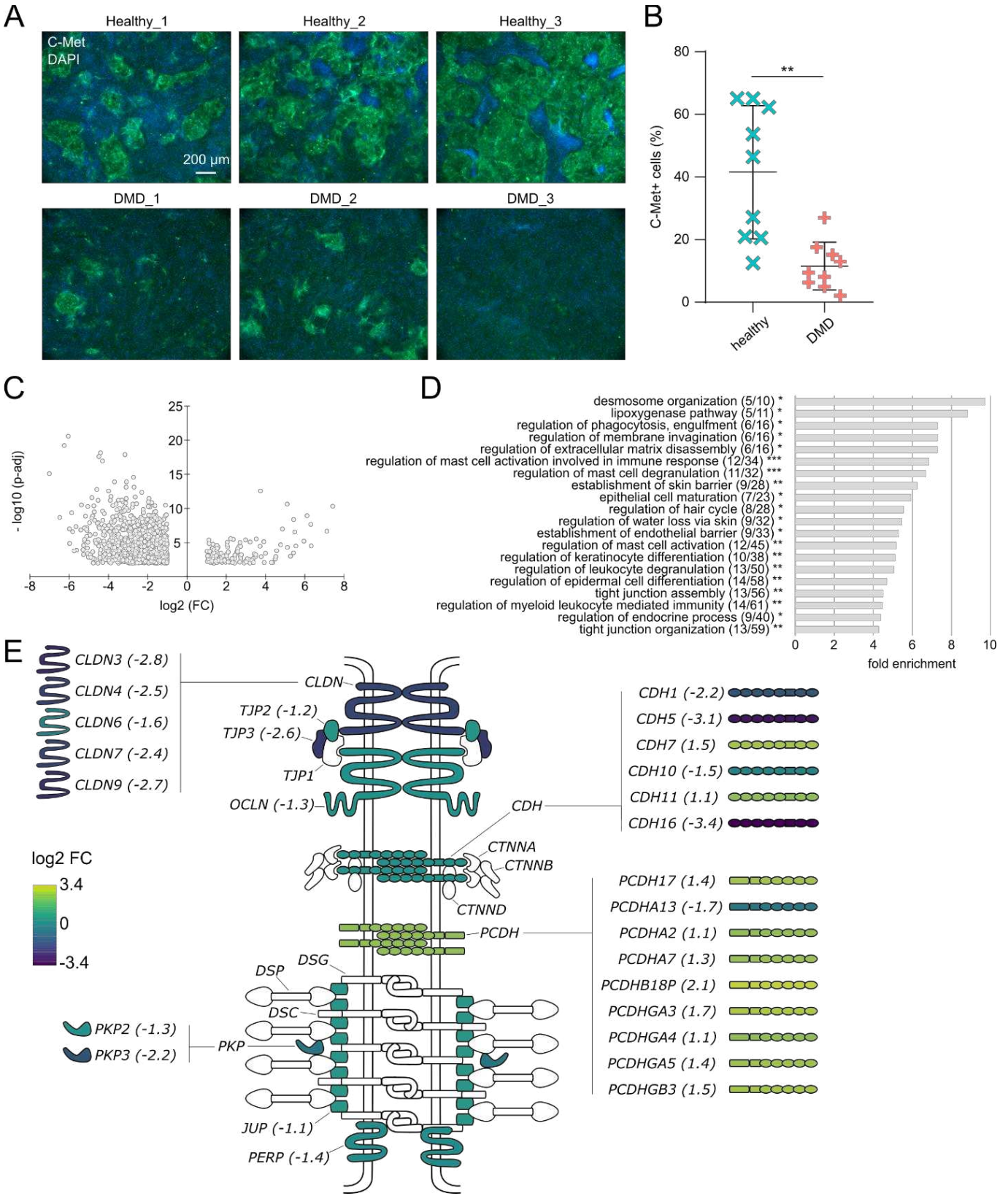

361

Figure 4: Somitogenesis and cell junction genes are dysregulated in three additional DMD hiPSC lines. (A) Fluorescent staining of C-Met in DMD hiPSCs and healthy control lines at Day 10 of the myogenic differentiation. One representative picture is shown per individual line (Healthy_1 to 3 and DMD_1 to 3). (B) Quantification of the C-Met fluorescent area normalized by the number of nuclei. Imaging was performed on three independent pictures per line. (C) Volcano plot of the differentially expressed genes in DMD somite progenitor cells at Day 10 (thresholds: |log2 FC| > 1 & p-adj < 0.01). (D) Gene Ontology analysis using the differentially expressed genes as input and showing key biological processes. Legend: * false discovery rate (FDR) < 0.05; ** FDR < 0.01; *** FDR < 0.001; (X/Y): number of genes from the GO category found differentially expressed in the dataset / total number of genes in the GO category. (E) Differential expression of cell junction genes and potential implications at the protein level. Fold change values (DMD vs. Healthy) are indicated between brackets and color-coded for each protein. CLDN: claudin; OCLN: occludin; TJP: tight junction protein; CDH: cadherin; CTNN: contactin; PCDH: protocadherin; DSG: desmoglein; DSP: desmoplakin; DSC: desmocollin; PKP: plakophilin; JUP: plakoglobin; PERP: p53 apoptosis effector related to PMP22.

Material & Methods

RESOURCE AVAILABILITY

Lead contact

Further information and requests for resources and reagents should be directly addressed to and will be fulfilled by the lead contact, Jean-Baptiste Dupont (jean-baptiste.dupont@univ-nantes.fr).

Materials availability

This study did not generate new unique reagents

Data and code availability

- The two single-cell RNA-seq data sets have been deposited at GEO and are publicly available as of the date of publication. Accession numbers are listed in the key resources table. This paper also analyzes publicly available data. These accession numbers are listed in the key resources table. Original western blot images and microscopy data reported in this paper have been deposited at Zenodo repository. DOIs are listed in the key resources table.

- All original code has been deposited as R Notebook files at Zenodo Repository. DOIs are listed in the key resources table.

- Any additional information required to reanalyze the data reported in this paper is available from the lead contact upon request.

EXPERIMENTAL MODEL AND STUDY PARTICIPANT DETAILS

Ethical statement: The Healthy, DMD and CRISPR lines have been described, characterized and published previously[34,37]. Participants gave informed consent for the generation of urine-derived hiPSC lines, as required by the Institutional Review Board (IRB). The experiments performed in this manuscript fall into the

Category 1A described in the Guidelines for Stem Cell Research and Clinical Translation of the International Society for Stem Cell Research (ISSCR, https://www.isscr.org/guidelines).

hiPSC lines: The Healthy UC3-4 line was generated from an adult male participant with no known skeletal muscle disease. The DMD 72039 line was generated from an adult male with a declared DMD pathology and carrying an exon50 deletion in the *DMD* gene. These individuals provided urine samples, from which urine cells were expanded and reprogrammed to generate hiPSCs by Guan X. *et al.* at the University of Washington, Seattle (USA)[34]. The DMD CRISPR line was generated from the UC3-4 line by CRISPR Cas 9 gene editing by Smith A. *et al.* in collaboration with the Institute for Stem Cell and Regenerative Medicine Ellison Stem Cell Core[37]. It carries an exon 45 deletion and a 17 bp deletion in exon 54 of the *DMD* gene. The absence of dystrophin was confirmed by Western blot after myogenic differentiation, in comparison with the Healthy UC3-4 control line (Figure S2A). Cell lines were not otherwise authenticated. The three hiPSC lines were extensively characterized, expanded and shared with the TaRGeT INSERM laboratory at Nantes Université through a dedicated Material Transfer Agreement.

hiPSC maintenance: All cell culture experiments were performed at 37 °C and 5 % CO2 in a standard tissue culture incubator. The three hiPSC lines were expanded in the TaRGeT laboratory as Master Cell Banks (MCB) at various passages (Healthy: passage 34; DMD: passage 25; CRISPR: passage 46). Cells were thawed at 37°C and seeded as clusters on Matrigel-coated plates (1:60 dilution) after spinning 3 min at 300 g and resuspension in mTeSR Plus culture medium supplemented in 10 µM ROCK inhibitor. Fresh media without ROCK inhibitor was renewed the day after seeding and then every other day. Cultures were manually cleaned from abnormally looking clusters and were passaged with Versene when the overall confluence reached 70 – 80 %. Working Cell Banks (WCB) were stored after two passages from the MCBs. Cells were detached with Versene, spun down 3 min at 300 g, and clusters were gently resuspended in Cryostor freezing media for long term cryopreservation in liquid nitrogen.

Rat Muscle biopsies: The protein samples used as positive controls in the dystrophin western-blot were obtained from rat pectoral muscle biopsies from a previous study[58]. Dmd^{mdx} rats and healthy controls were handled and housed in the UTE IRS2 from Nantes Université, according to a protocol approved by the Institutional Animal Care and Use Committee of the Région des Pays de la Loire (University of Angers,

France) as well as the French Ministry for National Education, Higher Education and Research (authorization #2018102616384887).

METHOD DETAILS

hiPSC myogenic differentiation: This study combines the use of two myogenic differentiation protocols:

- Establishment of the myogenic trajectory: hiPSCs were differentiated with a succession of five defined media, as published previously[15]. After seeding on Matrigel (1:60 dilution) as single cells at a density of 30,000 cells / cm², hiPSCs were grown for 2 – 3 days in mTeSR Plus media. ROCK inhibitor was added upon seeding but removed by a fresh media change after one day. The cells were then incubated in five successive differentiation media based on Dulbecco's Modified Eagle's Medium (DMEM) / F12 supplemented with Non-Essential Amino Acids (NEAA) and additional molecules detailed below:
  - Media 1 (3 days): Insulin transferrin selenium (ITS) 1X + 3 µM CHIR99021 + 0.5 µM LDN
  - Media 2 (3 days): Insulin transferrin selenium (ITS) 1X + 3 µM CHIR99021 + 0.5 µM LDN + basic Fibroblast Growth Factor (bFGF) at 20 µg / ml
  - Media 3 (2 days): 15 % Knockout serum replacement (KSR) + 0.5 µM LDN + bFGF at 20 µg / ml + Hepatocyte Growth Factor (HGF) at 10 µg / ml + Insulin-like Growth Factor (IGF) 1 at 2 ng / ml.
  - Media 4 (4 days): 15 % KSR + IGF-1 at 2 ng / ml
  - Media 5 (16 days): 15 % KSR + IGF-1 at 2 ng / ml + HGF at 10 µg / ml

  Cells were collected at Day 0, 1, 2, 4, 7, 10, 14, 18, 22 and 28 after incubation with Trypsin-EDTA alone, or with a combination of Trypsin-EDTA + collagenase IV at 50 U / µl for 10 min at 37 °C, mechanical dissociation and passage through a 70 µm cell strainer to remove debris and extracellular matrix.
- Post hoc analysis of the somite differentiation stage at Day 10: in parallel, hiPSCs were differentiated with a commercially available media previously shown as capable of reproducing the somite stage with high accuracy[16,19]. This protocol uses lower initial seeding densities and allows for an easier visualization and imaging of the cultures as differentiation progresses. Briefly, hiPSCs

were first amplified and dissociated as single cells as described above, and then seeded on collagen I-coated plates at 3,500 cells / cm² in Skeletal Muscle Induction Medium (amsbio SKM01). The media was changed every 2 to 3 days. At Day 7, cells were dissociated with Trypsin-EDTA and cryopreserved in CryoStor CS10 medium. They were seeded on new collagen-coated plates at 20,000 cells / cm² in SKM01 until Day 10.

single-cell RNA-Seq:

- sci-RNA-Seq: the myogenic trajectory followed by hiPSCs was determined by single-cell combinatorial indexing RNA-Seq (sci-RNA-Seq) as previously published[35]. Cells were collected as differentiation progressed (5 to 10 million per sample, from Day 0 to Day 28) and spiked with 10 % murine cells of the NIH/3t3 cell line for estimation of doublet proportions. after centrifugation for 5 min at 300 g and 4 °C, pellets were washed in DPBS and resuspended in pre-chilled methanol for fixation and permeabilization. They were then stored at – 20°C until all samples were processed at the end of the differentiation. Fixed cells were pelleted by centrifugation (same settings), washed twice in 1 ml DPBS + 1 % Diethylpyrocarbonate (DEPC), and another three times in 1 ml of cell wash buffer containing 1 % SUPERase In RNase Inhibitor and 1 % BSA in ice-cold DPBS. The final resuspension was made in 100 µl of cell wash buffer before counting with a hemocytometer. The Reverse Transcription step was performed 10 min at 55 °C *in situ* on 2,000 cells per sample, with the Superscript IV RT kit and barcoded oligo dT primers dispatched in a Lo-bind 96-well plate. To increase the diversity of barcode combinations obtained after indexing, six distinct barcodes were used for the Day 0, Day 1 and Day 2 samples and four barcodes for the remaining samples (Day 4, Day 7, Day 10, Day 14, Day 18, Day 22, Day 28). The RT reaction was stopped with 40 mM EDTA and 1 mM spermidine (5 µl per well). Cells with barcoded cDNA were then pooled in a flow cytometry tube, stained with 300 µM DAPI and sorted in a new 96-well Lo-bind plate (25 cells per well) containing Elution buffer (5 µl per well). Sorting plates can be stored at – 80 °C after brief centrifugation. Second strand synthesis was performed in each well with the NEBNext® Ultra™ II Non-Directional RNA Second Strand Synthesis Module (0.5 µl of Buffer + 0.25 µl of enzyme per well). After incubation at 16 °C for 150 min, the reaction was terminated at 75 °C for 20 min.

Tagmentation was performed in each well with the illumina Tagment DNA TDE1 Enzyme (0.5 µl per well) and buffer (5 µl per well) kit, after addition of human genomic DNA (0.25 µl per well). The plate was incubated at 55 °C for 5 min and the reaction was stopped with 12 µl DNA binding buffer per well and incubation at room temperature (RT) for 5 min. AMPure XP beads (36 µl per well) were added for purification with standard protocol. The elution step was performed in a final volume of 17 µl. Libraries were amplified by PCR using the NEBNext High-Fidelity 2X PCR Master Mix and barcoded P5 primers (2 µl of 10 µM primer per well), in addition to a 10 µM P7 primer (2 µl per well). Amplification was carried out in a standard thermal cycler with the following program: 5 min at 72 °C + 30 sec at 98 °C + 18 cycles of (10 sec at 98 °C + 30 sec at 66 °C + 30 sec at 72 °C) + 5 min at 72 °C. Samples were collected from each well and pooled in a single tube. The library was then purified using 0.8 volume of AMPure XP beads according to manufacturer's instructions. Libraries were quantified by Qubit and visualized by electrophoresis on a 6 % TBE-PAGE gel. Sequencing was performed on the NextSeq 500 platform using a V2 75 cycles kit and the following settings: Read 1: 18 cycles, Read 2: 52 cycles, Index 1: 10 cycles, Index 2: 10 cycles. Here, two sorting plates were generated and used to generated independent libraries sequenced successively with distinct P7 primers. The first sorting plate was full and thus 96 barcoded P5 primers were used in the PCR amplification step; the second sorting plate only used 86 wells (and thus 86 barcoded P5 primers). The sequences of the barcoded primers used in this protocol can be found in Table S6. Raw data analysis involved base calling (bcl2fastq), demultiplexing based on P5 barcodes (1 mismatched base allowed), adaptor trimming (trim_galore), alignment to the human (hg19) or the mouse (mm10) genome (STAR), removing of UMI duplicates and demultiplexing based on RT barcodes. Percentages of reads mapping uniquely to the human and the mouse genome were quantified and cells with over 90 % of reads assigned to the human genome were kept for subsequent analysis. Secondary analysis of the cell data set object was performed with the Monocle 3 analysis pipeline (Trapnell 2014, Qiu 2017), whose code is freely available on the Cole Trapnell lab Github and in the Zenodo Repository with the DOI listed in the key resources table.

- split-pool barcoding: the *post hoc* analysis of the somite differentiation step at Day 10 was performed with the split-pool barcoding kit commercialized by parse Biosciences, according to manufacturer's instructions. Cells were collected at Day 10 and counted with a hemocytometer to isolate 500,000 cells for subsequent fixation and permeabilization with the Cell Fixation Kit. Samples were stored at – 80°C and thawed immediately prior to library preparation with the Evercode Whole Transcriptome Mini Kit. Primary analysis of the raw data including quality control, alignment to the human genome (hg19), demultiplexing and generation of the matrix, feature annotation and cell annotation files were carried out by the proprietary Parse Biosciences analysis suite. Secondary analysis used the Monocle 3 pipeline as previously indicated. The code has been deposited at Zenodo Repository with the DOI listed in the key resources table.

Immunofluorescence:

- Somite progenitors: hiPSCs were first differentiated into somite progenitor cells with the amsbio commercial protocol to constitute a working cell bank at Day 7. Subsequently, cryotubes containing one million progenitors were thawed and seeded at 23,500 cells/cm² on Lab-Tek™ 4-well chamber slides (Thermofisher Cat# 154526PK) coated with collagen I (1:60 dilution). Cells were maintained in Skeletal Muscle Induction medium supplemented with 2% Pen/Strep and incubated at 37°C, 5% CO2 until confluency.

- Myotubes: myogenic progenitors were differentiated from hiSPCs with the amsbio commercial protocol and banks were made at Day 17. Subsequently, cryotubes containing one million progenitors were thawed and seeded at 23,500 cells/cm² on Lab-Tek™ 4-well chamber slides (Thermofisher Cat# 154526PK) coated with collagen I (1:60 dilution). They were maintained in Skeletal Muscle Myoblast medium supplemented with 2% Pen/Strep and incubated at 37°C, 5% CO2 until confluency. Differentiation was induced with the Skeletal Muscle Myotube medium supplemented with 2% Pen/Strep for 8 days, with a fresh media change every 2 to 3 days.

Cells were fixed in 4 % paraformaldehyde (PFA) for 1 hr and then permeabilized in PBS + Triton 1X + 2.5% bovine serum albumin (BSA). Primay antibodies were diluted in permeabilization buffer and incubated on

the cells overnight at 4 °C (E-Cadherin Alexa Fluor™ 488, Vimentin eFluor™ 570 and C-Met: 1:50 dilution; Myosin Heavy Chain: 1:300 dilution; α-actinin: 1:500 dilution). The next day, nuclei were stained with 1:10.000 DAPI and for myotubes, the anti-mouse or anti-goat (C-Met) secondary antibodies were diluted at 1:1000 in PBS and added for 1 hr at RT. Coverslips were mounted on the slides using ProLong Gold Antifade Reagent after removing the Lab-Tek™ walls. Images were taken with a 20 X oil immersion objective on a NIKON® A1 RSi confocal microscope.

Western-blot: Proteins were extracted from frozen cell pellets in RIPA buffer during 1 hour (10 mM Tris + 150 Mm NaCl + 1mM protease inhibitor cocktails + 1% Igepal + 0.1% SDS). Protein extracts diluted at 1:10 were quantified with the DC Protein Assay kit at 750 nm on the Thermo Scientific™ Multiskan™ GO. Protein samples (50 µg per sample) were denatured by addition of NuPAGE LDS sample buffer 4X and Dithiothreitol (DTT), and loaded onto a Nupage 3-8% TA Gel before migrating for 2 hrs at 100 V in 1X NuPAGE tris acetate SDS buffer. Protein extracts from Healthy and DMD^{mdx} rat pectoral muscles were loaded as controls. The Bio-Rad Trans-Blot Turbo Transfer System was used for protein transfer. After overnight saturation at 4 °C in saturation buffer (5 % milk + 0.1 % Tween 20 + 1 % NP40), membranes were incubated with primary Mouse anti-dystrophin NCL-DYS2 antibody diluted at 1:250 for 1 hr. The α-tubulin protein was labeled with a Mouse Monoclonal Anti-α-Tubulin antibody diluted at 1:10000. All membranes were then washed three times for 5 minutes in PBS + 0.1 % Tween 20 before incubation with the corresponding secondary antibodies (Goat Anti-Mouse antibody/HRP diluted at 1 :5000 during 1 hr). The ECL kit was used for detection of the HRP enzyme activity, with exposure times of 2 minutes (α-tubulin) and 2 hours (Dystrophin).

QUANTIFICATION AND STATISTICAL ANALYSIS

Immunofluorescence: Each hiPSC line was differentiated and imaged as 4 by 4 panels or individual pictures, and analyzed with the QuPath software. C-Met and Ecad-positive areas were determined by thresholding on the Alexa488 fluorescent channel (ECad: Threshold = 40 or regions manually drawn if low signal, C-Met: Threshold = 600, minimal object size= 2,500 µm²), and the number of nuclei was determined in the positive and negative areas using the Cell Detection tool with the following parameters: C-Met: DAPI

threshold = 100, object size between 10 and 400 µm², background radius = 8 µm, sigma = 1.5 µm; E-Cad: DAPI threshold = 100, object size between 75 and 2000 µm², background radius = 8 µm, sigma = 2 µm. E-Cad pictures were acquired at higher magnification, explaining why different parameters had to be used. MF20- and a-actinin-positive areas were determined by thresholding on the TRITC channel (MF20: threshold = 100, α-actinin: threshold = 1000). Data were represented and analyzed with GraphPad PRISM 8.0.1. Non-parametric statistical tests were used to compare groups as sample size were low and we could not assume gaussian distributions nor homoscedasticity. The Mann-Whitney statistics was used when only two groups were compared, and the Kruskal-Wallis statistics for comparison of the 3 groups.

KEY RESOURCES TABLE

REAGENT or RESOURCE	SOURCE	IDENTIFIER
Antibodies		
Myosin heavy chain	DSHB	Cat# MF20 RRID:AB_2147781
alpha-Actinin (Sarcomeric)	Sigma-Aldrich	Cat# A7811; RRID:AB_476766
CD324 (E-cadherin) Alexa Fluor™ 488	Thermo Fisher	Cat# 53-3249-80 RRID:AB_10671270
Vimentin eFluor™ 570	Thermo Fisher	Cat# 41-9897-80 RRID:AB_11220476
Human HGFR/c-MET	R&D Systems	Cat# AF276 RRID:AB_355289
Goat anti-Mouse IgG2b Alexa Fluor™ 555	Thermo Fisher	Cat# A-21147 RRID:AB_2535783
Donkey anti-Goat IgG Alexa Fluor™ 488	Thermo Fisher	Cat# A-11055 RRID:AB_2534102
Dystrophin	Leica	Cat# NCL-DYS2 RRID:AB_442081
GAPDH	Novus	Cat# NB300-320 RRID:AB_10001796
Alpha tubulin	Sigma-Aldrich	Cat# T5168 RRID:AB_477579
Goat Anti-Mouse Immunoglobulins/HRP	Agilent	Cat# P0447 RRID:AB_2617137
Polyclonal Rabbit Anti-Goat Immunoglobulins/HRP	Agilent	Cat# P0449 RRID:AB_2617143
Chemicals, peptides, and recombinant proteins		
mTeSR™ Plus	STEMCELL Technologies	Cat# 100-0276
Matrigel® Matrix	Corning	Cat# 354234
Versene solution	Thermo Fisher	Cat# 15040066
CryoStor CS10 cryopreservation medium	STEMCELL Technologies	Cat# 07959
DPBS	Thermo Fisher	Cat# 14190144
Y-27632 ROCK inhibitor	Selleckchem	Cat# S1049

DMEM/F12	Thermo Fisher	Cat# 11320033
CHIR99021	STEMCELL Technologies	Cat# 72054
StemMACS™ LDN-193189	Miltenyi Biotec	Cat# 130-103-925
Recombinant Human FGF2	R&D Systems	Cat# 233-FB-010
Recombinant Human IGF-1	R&D Systems	Cat# 291-G1-200
Recombinant Human HGF	R&D Systems	Cat# 294-HG-005
KnockOut™ serum replacement	Thermo Fisher	Cat# 10828010
Collagenase, type IV	Thermo Fisher	Cat# 1710419
Trypsin-EDTA	Sigma-Aldrich	Cat# T4174
Skeletal Muscle. Induction Medium	amsbio	Cat# SKM01
Skeletal Muscle. Myoblast Medium	amsbio	Cat# SKM02
Skeletal Muscle. Myotube Medium	Amsbio	Cat# SKM03
Cultrex Rat Collagen I	R&D Systems	Cat# 3440-100-01
Paraformaldehyde	Thermo Fisher	Cat# #28906
Triton 100X	Eurobio	Cat# GAUTTR001
BSA (immunofluorescence)	Sigma-Aldrich	Cat# A3059
ProLong™ Gold Antifade reagent	Thermo Fisher	Cat# P36934
Tris base	Sigma-Aldrich	Cat# 10708976001
cOmplete™ Protease Inihibitor Cocktail	Merck	Cat# 11873580001
Protease inhibitor cocktail	Sigma-Aldrich	Cat# P8340
Igepal CA-630	Sigma-Aldrich	Cat# I3021
SDS solution	Sigma-Aldrich	Cat# 05030
NuPAGE™ LDS sample buffer	Thermo Fisher	Cat# NP0007
Dithiothreitol	Thermo Fisher	Cat# D1532
NuPAGE™ Tris-acetate Gel	Thermo Fisher	Cat# EA03785BOX
NuPAGE™ Tris acetate SDS buffer	Thermo Fisher	Cat# LA0041
Tween 20	Merck	Cat# 8170721000
Pierce™ ECL Western Blotting Substrate	Thermo Fisher	Cat# 32106
Nuclease free water	Ambion	Cat# AM9932
Methanol	Fisher Scientific	Cat# 10285131
SUPERase In RNase inhibitor	Invitrogen	Cat# AM2694
BSA (single-cell RNA-Seq)	New England Biolabs	Cat# B9000
1M Tris-HCl pH 7.5	Thermo Fisher	Cat# 15567027
5M NaCl (single-cell RNA-Seq)	Thermo Fisher	Cat# AM9759
1M MgCl2	Thermo Fisher	Cat# AM9530G
IGEPAL CA-360	Sigma-Aldrich	Cat# 18896
Diethyl pyrocarbonate	Sigma-Aldrich	Cat# D5758
10mM dNTP	Thermo Fisher	Cat# 18427013
Superscript IV reverse transcriptase	Thermo Fisher	Cat# 18090200
RNaseOUT Recombinant Ribonuclease Inhibitor	Thermo Fisher	Cat#10777019
0.5M EDTA pH 8.0	Thermo Fisher	Cat# 15575020
Spermidine	MP Biomedicals	Cat# 0219485201
Elution Buffer	Qiagen	Cat# 19086
DAPI	Thermo Fisher	Cat# D1306
DNA binding buffer	Zymo Research	Cat# D4003-1
AMPure XP beads	Beckman Coulter	Cat# A63880
Ethanol	Decon Labs	Cat# 2716
NEBNext® High Fidelity 2X PCR Master Mix	New England Biolabs	Cat# M0541

Novex® TBE-PAGE gels, 6%	Thermo Fisher	Cat# EC6265BOX
Quick-Load 2-log DNA Ladder	New England Biolabs	Cat# N0550
Critical commercial assays		
Nextseq 500/550 V2 75 cycle kit	illumina	Cat# 20024906
DC Protein Assay	Bio-Rad	Cat# 5000111
Tagment DNA TDE1 Enzyme and Buffer Kit	illumina	Cat# 20034197
Evercode™ Whole Transcriptome Mini Kit	Parse Biosciences	Cat# EC-W01010
Cell Fixation Kit	Parse Biosciences	Cat# SB1001
Qubit dsDNA HS Kit	Thermo Fisher	Cat# Q32851
NEBNext® Ultra™ II Non-Directional RNA Second Strand Synthesis Module	New England Biolabs	Cat# E6111
Deposited data		
sciRNA-Seq myogenesis time course data	This paper	GEO accession number: GSE233605
Bulk RNA Seq Day 10 data	Mournetas *et al.*[1]	ArrayExpress: E-MTAB-8321
Split-pool barcoding scRNASeq Day 10 data	This paper	GEO accession number: GSE233606
Supplementary Tables S1 to S6	This paper	Zenodo DOI: 10.5281/zenodo.8414351
Full Western blots films related to Figure S2A	This paper	Zenodo DOI: 10.5281/zenodo.7937310
Immunofluorescence pictures related to Figure 3A-B	This paper	Zenodo DOI: 10.5281/zenodo.8325281
Immunofluorescence pictures related to Figure 3D-E	This paper	Zenodo DOI: 10.5281/zenodo.7950222
Immunofluorescence pictures related to Figure 3F-G	This paper	Zenodo DOI: 10.5281/zenodo.8325290
Immunofluorescence pictures related to Figure 4A-B	This paper	Zenodo DOI: 10.5281/zenodo.8325317
Experimental models: Cell lines		
UC3-4 Healthy hiPSC line, passage 32	Laboratory of David L Mack	N/A
DMD 72039 D3 hiPSC line, passage 22	Laboratory of David L Mack	N/A
UC3-4 DMD CRISPR hiPSC line, passage 41	Laboratory of David L Mack	N/A

NIH/3T3 cell spike (single-cell RNA-Seq)	ATCC	N/A
Oligonucleotides		
sciRNA-Seq barcoded oligonucleotides (see Table S1)	IDT	N/A
Custom P5 and P7 primers (see Table S1)	IDT	N/A
Software and algorithms		
Fiji (imageJ)	Schindelin *et al.*[2]	https://fiji.sc/
QuPath version 0.4.3	Bankhead *et al.*[3]	https://qupath.github.io/
PRISM version 8	Graphpad	https://www.graphpad.com/features
bcl2fastq version 2.16.0.10	illumina	https://emea.support.illumina.com/sequencing/sequencing_software/bcl2fastq-conversion-software.html
trim_galore version 0.4.5	Felix Krueger	https://www.bioinformatics.babraham.ac.uk/projects/trim_galore/
STAR version 2.5.2b	Dobin *et al.*[4]	https://github.com/alexdobin/STAR
R version 4.2.2	https://cran.r-project.org/	
dplyr version 1.1.0	Wickham *et al.*	https://dplyr.tidyverse.org/
monocle version 1.3.1	Cao *et al.*[5,6]	https://cole-trapnell-lab.github.io/monocle3/
ggplot2 version 3.1.4	Wickham *et al.*	https://ggplot2.tidyverse.org/
sci-RNA-Seq and split-pool barcoding analysis pipelines	This paper	Zenodo DOI : 10.5281/zenodo.8348000

566

Supplemental references:

1. Mournetas, V., Massouridès, E., Dupont, J.-B., Kornobis, E., Polvèche, H., Jarrige, M., Dorval, A.R.L., Gosselin, M.R.F., Manousopoulou, A., Garbis, S.D., et al. (2021). Myogenesis modelled by human pluripotent stem cells: a multi-omic study of Duchenne myopathy early onset. J Cachexia Sarcopenia Muscle *12*, 209–232. 10.1002/jcsm.12665.

2. Schindelin, J., Arganda-Carreras, I., Frise, E., Kaynig, V., Longair, M., Pietzsch, T., Preibisch, S., Rueden, C., Saalfeld, S., Schmid, B., et al. (2012). Fiji: an open-source platform for biological-image analysis. Nat Methods *9*, 676–682. 10.1038/nmeth.2019.

3. Bankhead, P., Loughrey, M.B., Fernández, J.A., Dombrowski, Y., McArt, D.G., Dunne, P.D., McQuaid, S., Gray, R.T., Murray, L.J., Coleman, H.G., et al. (2017). QuPath: Open source software for digital pathology image analysis. Sci Rep *7*, 16878. 10.1038/s41598-017-17204-5.

4. Dobin, A., Davis, C.A., Schlesinger, F., Drenkow, J., Zaleski, C., Jha, S., Batut, P., Chaisson, M., and Gingeras, T.R. (2013). STAR: ultrafast universal RNA-seq aligner. Bioinformatics *29*, 15–21. 10.1093/bioinformatics/bts635.

5. Cao, J., Packer, J.S., Ramani, V., Cusanovich, D.A., Huynh, C., Daza, R., Qiu, X., Lee, C., Furlan, S.N., Steemers, F.J., et al. (2017). Comprehensive single-cell transcriptional profiling of a multicellular organism. Science *357*, 661–667. 10.1126/science.aam8940.

6. J, C., M, S., X, Q., X, H., Dm, I., Aj, H., F, Z., S, M., L, C., Fj, S., et al. (2019). The single-cell transcriptional landscape of mammalian organogenesis. Nature *566*. 10.1038/s41586-019-0969-x.

Supplemental information

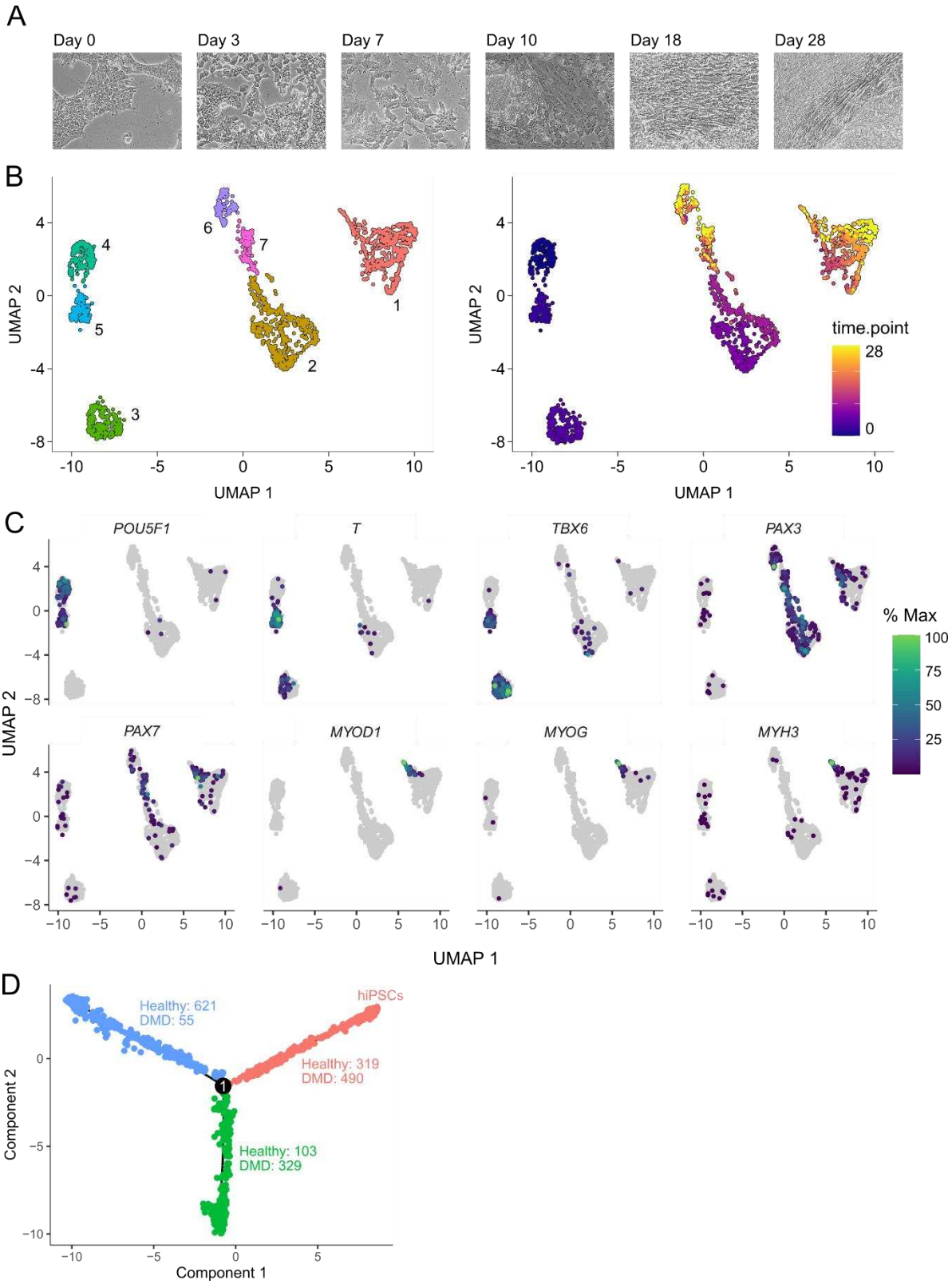

589 **Supplemental Figure S1:** Myogenic differentiation of hiPSCs at the single-cell resolution. (A) Observation
590 of hiPSC cultures along the differentiation at process by phase contrast microscopy. (B) UMAP plot showing
591 the 1917 individual cells colored by cluster (left panel) and by collection time point from Day 0 to D28 (right
592 panel). (C) Expression of successive developmental markers in hiPSCs along the myogenic differentiation.
593 (D) Number of DMD and Healthy cells on the three branches of the developmental trajectory.

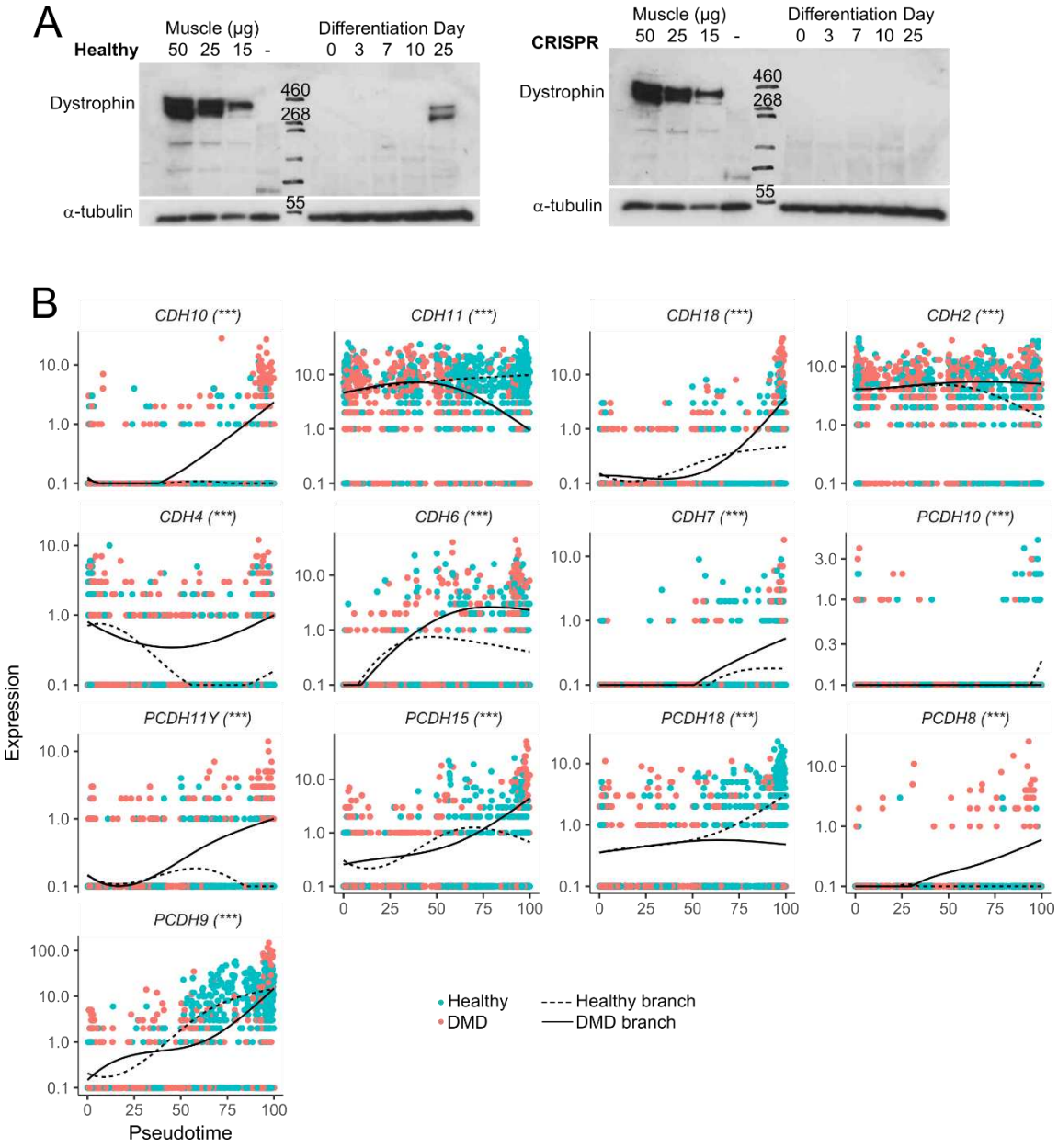

Supplemental Figure S2: (A) Expression of dystrophin along the myogenic differentiation of CRISPR hiPSCs (right panel) and healthy control cells (left panel). Proteins were extracted from cell samples collected from Day 0 to Day 25 or from the pectoral muscles of a healthy rat as positive controls ("Muscle") and a Dmd^{mdx} rat as a negative control ("-"), and subjected to anti-dystrophin western-blot analysis. Alpha tubulin (a-tubulin) was used as a control. (B) Pseudotime expression of *CDH* and *PCDH* along the Healthy and the DMD branches in the sci-RNA-Seq data set. Individual cells are colored by their hiPSC line of origin and ordered along the pseudotime axis. BEAM statistics: ***: adjusted p-value < 0.001.

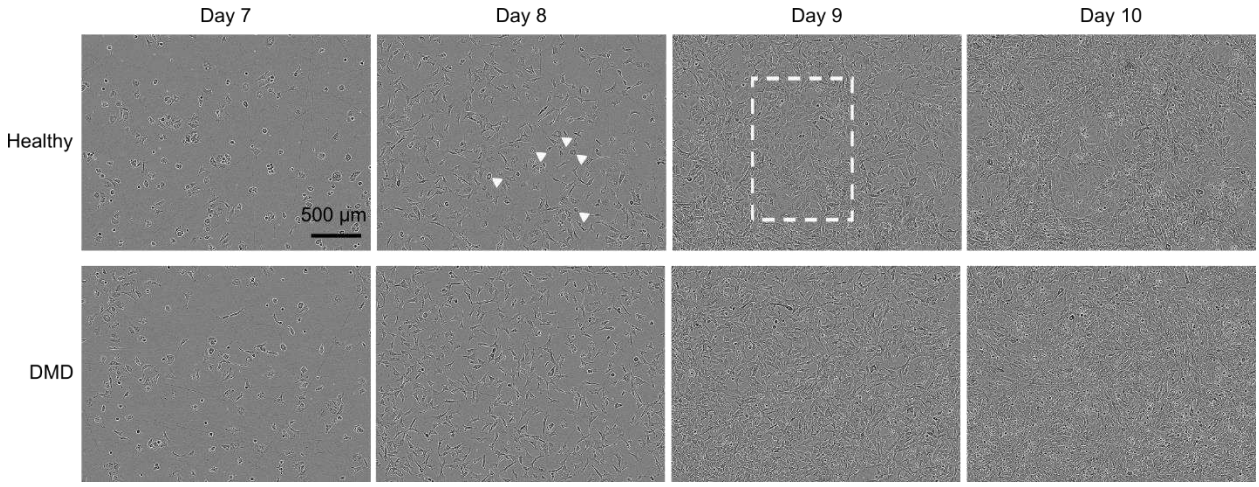

602

603 **Supplemental Figure S3:** Evolution of hiPSC cultures between Day 7 and Day 10 of the myogenic
604 differentiation protocol. Arrowheads indicate “round” cells appearing from Day 8 and at the core of the
605 epithelial islets visible from Day 9 – Day 10 (white rectangle).

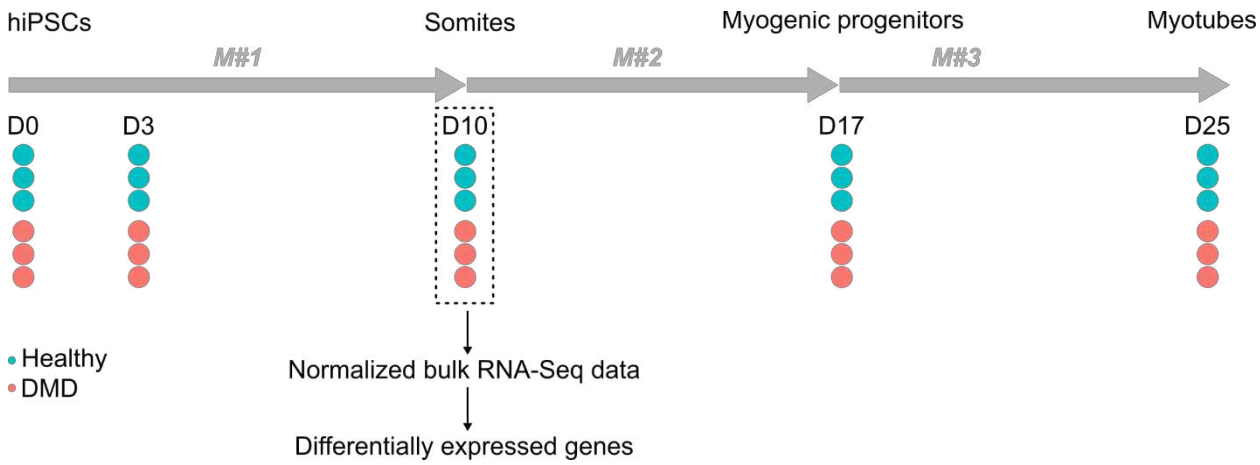

606

607 **Supplemental Figure S4:** Differentiation of DMD and Healthy hiPSCs and cell collection protocol in the
608 analyzed study[19]. Each individual line is indicated by a blue (Healthy) or a red (DMD) dot, and the analysis
609 at Day 10 is highlighted by a dotted square.

Supplemental Table S1: cell_data file obtained after the initial sciRNA-Seq experiment. The genotype, time point, number of expressed genes and cluster of origin are indicated for each individual cell.

Supplemental Table S2: Differentially expressed genes (p-adj < 0.0001) obtained after branch expression analysis modeling (BEAM) and the cluster to which they belong on the heatmap shown in Figure 1F.

Supplemental Table S3: Differentially expressed genes (p-adj < 0.01) detected at Day 10 after sciRNA-Seq.

Supplemental Table S4: Differentially expressed genes (p-adj < 0.01) detected at Day 10 after split-pool barcoding RNA-Seq.

Supplemental Table S5: Differentially expressed genes (abs(log2(fold-change)) > 1 & p-adj < 0.01) detected at Day 10 after bulk RNA-Seq in our previous study[19].

Supplemental Table S6: List of barcoded primers used in the RT reaction and in the illumine library preparation of the sciRNA-Seq experiment.

The Supplementary Tables S1 to S6 have been deposited on the Zenodo database, and are available using the following DOI: 10.5281/zenodo.8414351

References:

1. Bushby, K., Finkel, R., Birnkrant, D.J., Case, L.E., Clemens, P.R., Cripe, L., Kaul, A., Kinnett, K., McDonald, C., Pandya, S., et al. (2010). Diagnosis and management of Duchenne muscular dystrophy, part 1: diagnosis, and pharmacological and psychosocial management. Lancet Neurol *9*, 77–93. 10.1016/S1474-4422(09)70271-6.

2. Wang, C.H., Bonnemann, C.G., Rutkowski, A., Sejersen, T., Bellini, J., Battista, V., Florence, J.M., Schara, U., Schuler, P.M., Wahbi, K., et al. (2010). Consensus statement on standard of care for congenital muscular dystrophies. J. Child Neurol. *25*, 1559–1581. 10.1177/0883073810381924.

3. Wang, C.H., Dowling, J.J., North, K., Schroth, M.K., Sejersen, T., Shapiro, F., Bellini, J., Weiss, H., Guillet, M., Amburgey, K., et al. (2012). Consensus statement on standard of care for congenital myopathies. J. Child Neurol. *27*, 363–382. 10.1177/0883073812436605.

4. Duan, D., Goemans, N., Takeda, S., Mercuri, E., and Aartsma-Rus, A. (2021). Duchenne muscular dystrophy. Nat Rev Dis Primers *7*, 1–19. 10.1038/s41572-021-00248-3.

5. Nguyen, F., Cherel, Y., Guigand, L., Goubault-Leroux, I., and Wyers, M. (2002). Muscle lesions associated with dystrophin deficiency in neonatal golden retriever puppies. J. Comp. Pathol. *126*, 100–108. 10.1053/jcpa.2001.0526.

6. Merrick, D., Stadler, L.K.J., Larner, D., and Smith, J. (2009). Muscular dystrophy begins early in embryonic development deriving from stem cell loss and disrupted skeletal muscle formation. Dis Model Mech *2*, 374–388. 10.1242/dmm.001008.

7. Toop, J., and Emery, A.E. (1974). Muscle histology in fetuses at risk for Duchenne muscular dystrophy. Clin. Genet. *5*, 230–233.

8. Emery, A.E. (1977). Muscle histology and creatine kinase levels in the foetus in Duchenne muscular dystrophy. Nature *266*, 472–473. 10.1038/266472a0.

9. Pourquié, O., Al Tanoury, Z., and Chal, J. (2018). The Long Road to Making Muscle In Vitro. Curr Top Dev Biol *129*, 123–142. 10.1016/bs.ctdb.2018.03.003.

10. Linker, C., Lesbros, C., Gros, J., Burrus, L.W., Rawls, A., and Marcelle, C. (2005). beta-Catenin-dependent Wnt signalling controls the epithelial organisation of somites through the activation of paraxis. Development *132*, 3895–3905. 10.1242/dev.01961.

11. Rowton, M., Ramos, P., Anderson, D.M., Rhee, J.M., Cunliffe, H.E., and Rawls, A. (2013). Regulation of mesenchymal-to-epithelial transition by PARAXIS during somitogenesis. Developmental Dynamics *242*, 1332–1344. 10.1002/dvdy.24033.

12. Zhou, Y., Zhang, Y., and Zhu, D. (2018). Myostatin promotes the epithelial-to-mesenchymal transition of the dermomyotome during somitogenesis. Developmental Dynamics *247*, 1241–1252. 10.1002/dvdy.24681.

13. Avior, Y., Sagi, I., and Benvenisty, N. (2016). Pluripotent stem cells in disease modelling and drug discovery. Nat Rev Mol Cell Biol *17*, 170–182. 10.1038/nrm.2015.27.

14. Karagiannis, P., Takahashi, K., Saito, M., Yoshida, Y., Okita, K., Watanabe, A., Inoue, H., Yamashita, J.K., Todani, M., Nakagawa, M., et al. (2019). Induced Pluripotent Stem Cells

663 and Their Use in Human Models of Disease and Development. Physiological Reviews *99*, 79–
664 114. 10.1152/physrev.00039.2017.

665 15. Chal, J., Al Tanoury, Z., Hestin, M., Gobert, B., Aivio, S., Hick, A., Cherrier, T., Nesmith,
666 A.P., Parker, K.K., and Pourquié, O. (2016). Generation of human muscle fibers and satellite-
667 like cells from human pluripotent stem cells in vitro. Nat Protoc *11*, 1833–1850.
668 10.1038/nprot.2016.110.

669 16. Caron, L., Kher, D., Lee, K.L., McKernan, R., Dumevska, B., Hidalgo, A., Li, J., Yang, H.,
670 Main, H., Ferri, G., et al. (2016). A Human Pluripotent Stem Cell Model of Facioscapulohumeral
671 Muscular Dystrophy-Affected Skeletal Muscles. Stem Cells Transl Med *5*, 1145–1161.
672 10.5966/sctm.2015-0224.

673 17. Choi, I.Y., Lim, H., Estrellas, K., Mula, J., Cohen, T.V., Zhang, Y., Donnelly, C.J.,
674 Richard, J.-P., Kim, Y.J., Kim, H., et al. (2016). Concordant but Varied Phenotypes among
675 Duchenne Muscular Dystrophy Patient-Specific Myoblasts Derived using a Human iPSC-Based
676 Model. Cell Rep *15*, 2301–2312. 10.1016/j.celrep.2016.05.016.

677 18. Xi, H., Fujiwara, W., Gonzalez, K., Jan, M., Liebscher, S., Van Handel, B., Schenke-
678 Layland, K., and Pyle, A.D. (2017). In Vivo Human Somitogenesis Guides Somite Development
679 from hPSCs. Cell Rep *18*, 1573–1585. 10.1016/j.celrep.2017.01.040.

680 19. Mournetas, V., Massouridès, E., Dupont, J.-B., Kornobis, E., Polvèche, H., Jarrige, M.,
681 Dorval, A.R.L., Gosselin, M.R.F., Manousopoulou, A., Garbis, S.D., et al. (2021). Myogenesis
682 modelled by human pluripotent stem cells: a multi-omic study of Duchenne myopathy early
683 onset. J Cachexia Sarcopenia Muscle *12*, 209–232. 10.1002/jcsm.12665.

684 20. Massouridès, E., Polentes, J., Mangeot, P.-E., Mournetas, V., Nectoux, J., Deburgrave,
685 N., Nusbaum, P., Leturcq, F., Popplewell, L., Dickson, G., et al. (2015). Dp412e: a novel human
686 embryonic dystrophin isoform induced by BMP4 in early differentiated cells. Skelet Muscle *5*,
687 40. 10.1186/s13395-015-0062-6.

688 21. J, C., M, S., X, Q., X, H., Dm, I., Aj, H., F, Z., S, M., L, C., Fj, S., et al. (2019). The single-
689 cell transcriptional landscape of mammalian organogenesis. Nature *566*. 10.1038/s41586-019-
690 0969-x.

691 22. Xi, H., Langerman, J., Sabri, S., Chien, P., Young, C.S., Younesi, S., Hicks, M.,
692 Gonzalez, K., Fujiwara, W., Marzi, J., et al. (2020). A Human Skeletal Muscle Atlas Identifies the
693 Trajectories of Stem and Progenitor Cells across Development and from Human Pluripotent
694 Stem Cells. Cell Stem Cell *27*, 158-176.e10. 10.1016/j.stem.2020.04.017.

695 23. Giordani, L., He, G.J., Negroni, E., Sakai, H., Law, J.Y.C., Siu, M.M., Wan, R., Corneau,
696 A., Tajbakhsh, S., Cheung, T.H., et al. (2019). High-Dimensional Single-Cell Cartography
697 Reveals Novel Skeletal Muscle-Resident Cell Populations. Mol Cell *74*, 609-621.e6.
698 10.1016/j.molcel.2019.02.026.

699 24. Dos Santos, M., Backer, S., Saintpierre, B., Izac, B., Andrieu, M., Letourneur, F., Relaix,
700 F., Sotiropoulos, A., and Maire, P. (2020). Single-nucleus RNA-seq and FISH identify
701 coordinated transcriptional activity in mammalian myofibers. Nat Commun *11*, 5102.
702 10.1038/s41467-020-18789-8.

25. De Micheli, A.J., Spector, J.A., Elemento, O., and Cosgrove, B.D. (2020). A reference single-cell transcriptomic atlas of human skeletal muscle tissue reveals bifurcated muscle stem cell populations. Skelet Muscle *10*, 19. 10.1186/s13395-020-00236-3.

26. Kimmel, J.C., Yi, N., Roy, M., Hendrickson, D.G., and Kelley, D.R. (2021). Differentiation reveals latent features of aging and an energy barrier in murine myogenesis. Cell Rep *35*, 109046. 10.1016/j.celrep.2021.109046.

27. Mj, P., Co, S., C, S., K, C., X, C., Mt, W., N, S., and Dp, M. (2020). Single-nucleus RNA-seq identifies transcriptional heterogeneity in multinucleated skeletal myofibers. Nature communications *11*. 10.1038/s41467-020-20063-w.

28. Chemello, F., Wang, Z., Li, H., McAnally, J.R., Liu, N., Bassel-Duby, R., and Olson, E.N. (2020). Degenerative and regenerative pathways underlying Duchenne muscular dystrophy revealed by single-nucleus RNA sequencing. Proceedings of the National Academy of Sciences *117*, 29691–29701. 10.1073/pnas.2018391117.

29. Saleh, K.K., Xi, H., Switzler, C., Skuratovsky, E., Romero, M.A., Chien, P., Gibbs, D., Gane, L., Hicks, M.R., Spencer, M.J., et al. (2022). Single cell sequencing maps skeletal muscle cellular diversity as disease severity increases in dystrophic mouse models. iScience *25*, 105415. 10.1016/j.isci.2022.105415.

30. Scripture-Adams, D.D., Chesmore, K.N., Barthélémy, F., Wang, R.T., Nieves-Rodriguez, S., Wang, D.W., Mokhonova, E.I., Douine, E.D., Wan, J., Little, I., et al. (2022). Single nuclei transcriptomics of muscle reveals intra-muscular cell dynamics linked to dystrophin loss and rescue. Commun Biol *5*, 989. 10.1038/s42003-022-03938-0.

31. Taglietti, V., Kefi, K., Bronisz-Budzyńska, I., Mirciloglu, B., Rodrigues, M., Cardone, N., Coulpier, F., Periou, B., Gentil, C., Goddard, M., et al. (2022). Duchenne muscular dystrophy trajectory in R-DMDdel52 preclinical rat model identifies COMP as biomarker of fibrosis. Acta Neuropathol Commun *10*, 60. 10.1186/s40478-022-01355-2.

32. Trapnell, C., Cacchiarelli, D., Grimsby, J., Pokharel, P., Li, S., Morse, M., Lennon, N.J., Livak, K.J., Mikkelsen, T.S., and Rinn, J.L. (2014). The dynamics and regulators of cell fate decisions are revealed by pseudotemporal ordering of single cells. Nat. Biotechnol. *32*, 381–386. 10.1038/nbt.2859.

33. Qiu, X., Mao, Q., Tang, Y., Wang, L., Chawla, R., Pliner, H.A., and Trapnell, C. (2017). Reversed graph embedding resolves complex single-cell trajectories. Nat. Methods *14*, 979–982. 10.1038/nmeth.4402.

34. Guan, X., Mack, D.L., Moreno, C.M., Strande, J.L., Mathieu, J., Shi, Y., Markert, C.D., Wang, Z., Liu, G., Lawlor, M.W., et al. (2014). Dystrophin-deficient cardiomyocytes derived from human urine: new biologic reagents for drug discovery. Stem Cell Res *12*, 467–480. 10.1016/j.scr.2013.12.004.

35. Cao, J., Packer, J.S., Ramani, V., Cusanovich, D.A., Huynh, C., Daza, R., Qiu, X., Lee, C., Furlan, S.N., Steemers, F.J., et al. (2017). Comprehensive single-cell transcriptional profiling of a multicellular organism. Science *357*, 661–667. 10.1126/science.aam8940.

36. Kim, J., Magli, A., Chan, S.S.K., Oliveira, V.K.P., Wu, J., Darabi, R., Kyba, M., and Perlingeiro, R.C.R. (2017). Expansion and Purification Are Critical for the Therapeutic

744 Application of Pluripotent Stem Cell-Derived Myogenic Progenitors. Stem Cell Reports *9*, 12–22.
745 10.1016/j.stemcr.2017.04.022.

746 37. Smith, A.S., Luttrell, S.M., Dupont, J.-B., Gray, K., Lih, D., Fleming, J.W., Cunningham,
747 N.J., Jepson, S., Hesson, J., Mathieu, J., et al. (2022). High-throughput, real-time monitoring of
748 engineered skeletal muscle function using magnetic sensing. J Tissue Eng *13*,
749 20417314221122127. 10.1177/20417314221122127.

750 38. Thiery, J.P., Acloque, H., Huang, R.Y.J., and Nieto, M.A. (2009). Epithelial-
751 Mesenchymal Transitions in Development and Disease. Cell *139*, 871–890.
752 10.1016/j.cell.2009.11.007.

753 39. Dietrich, S., Abou-Rebyeh, F., Brohmann, H., Bladt, F., Sonnenberg-Riethmacher, E.,
754 Yamaai, T., Lumsden, A., Brand-Saberi, B., and Birchmeier, C. (1999). The role of SF/HGF and
755 c-Met in the development of skeletal muscle. Development *126*, 1621–1629.

756 40. Zhang, H., and Miller, R.H. (1995). Asynchronous differentiation of clonally related spinal
757 cord oligodendrocytes. Mol Cell Neurosci *6*, 16–31. 10.1006/mcne.1995.1003.

758 41. Pauklin, S., and Vallier, L. (2013). The Cell-Cycle State of Stem Cells Determines Cell
759 Fate Propensity. Cell *155*, 135–147. 10.1016/j.cell.2013.08.031.

760 42. Dong, C., Yang, X.-Z., Zhang, C.-Y., Liu, Y.-Y., Zhou, R.-B., Cheng, Q.-D., Yan, E.-K.,
761 and Yin, D.-C. (2017). Myocyte enhancer factor 2C and its directly-interacting proteins: A
762 review. Progress in Biophysics and Molecular Biology *126*, 22–30.
763 10.1016/j.pbiomolbio.2017.02.002.

764 43. Mérien, A., Tahraoui-Bories, J., Cailleret, M., Dupont, J.-B., Leteur, C., Polentes, J.,
765 Carteron, A., Polvèche, H., Concordet, J.-P., Pinset, C., et al. (2021). CRISPR gene editing in
766 pluripotent stem cells reveals the function of MBNL proteins during human in vitro myogenesis.
767 Hum Mol Genet, ddab218. 10.1093/hmg/ddab218.

768 44. Brent, A.E., and Tabin, C.J. (2002). Developmental regulation of somite derivatives:
769 muscle, cartilage and tendon. Current Opinion in Genetics & Development *12*, 548–557.
770 10.1016/S0959-437X(02)00339-8.

771 45. Weldon, S.A., and Münsterberg, A.E. (2022). Somite development and regionalisation of
772 the vertebral axial skeleton. Seminars in Cell & Developmental Biology *127*, 10–16.
773 10.1016/j.semcdb.2021.10.003.

774 46. Ordahl, C.P., Berdougo, E., Venters, S.J., and Denetclaw, W.F. (2001). The
775 dermomyotome dorsomedial lip drives growth and morphogenesis of both the primary myotome
776 and dermomyotome epithelium. Development *128*, 1731–1744. 10.1242/dev.128.10.1731.

777 47. Gros, J., Manceau, M., Thomé, V., and Marcelle, C. (2005). A common somitic origin for
778 embryonic muscle progenitors and satellite cells. Nature *435*, 954–958. 10.1038/nature03572.

779 48. Burgess, R., Rawls, A., Brown, D., Bradley, A., and Olson, E.N. (1996). Requirement of
780 the paraxis gene for somite formation and musculoskeletal patterning. Nature *384*, 570–573.
781 10.1038/384570a0.

49. Nakaya, Y., Kuroda, S., Katagiri, Y.T., Kaibuchi, K., and Takahashi, Y. (2004). Mesenchymal-epithelial transition during somitic segmentation is regulated by differential roles of Cdc42 and Rac1. Dev Cell *7*, 425–438. 10.1016/j.devcel.2004.08.003.

50. Feener, C.A., Koenig, M., and Kunkel, L.M. (1989). Alternative splicing of human dystrophin mRNA generates isoforms at the carboxy terminus. Nature *338*, 509–511. 10.1038/338509a0.

51. Bies, R.D., Phelps, S.F., Cortez, M.D., Roberts, R., Caskey, C.T., and Chamberlain, J.S. (1992). Human and murine dystrophin mRNA transcripts are differentially expressed during skeletal muscle, heart, and brain development. Nucleic Acids Research *20*, 1725–1731. 10.1093/nar/20.7.1725.

52. Muntoni, F., Torelli, S., and Ferlini, A. (2003). Dystrophin and mutations: one gene, several proteins, multiple phenotypes. The Lancet Neurology *2*, 731–740. 10.1016/S1474-4422(03)00585-4.

53. T, F., T, Y., H, T., and K, I. (2020). Dystroglycan regulates proper expression, submembranous localization and subsequent phosphorylation of Dp71 through physical interaction. Human molecular genetics *29*. 10.1093/hmg/ddaa217.

54. Romo-Yáñez, J., Rodríguez-Martínez, G., Aragón, J., Siqueiros-Márquez, L., Herrera-Salazar, A., Velasco, I., and Montanez, C. (2020). Characterization of the expression of dystrophins and dystrophin-associated proteins during embryonic neural stem/progenitor cell differentiation. Neurosci Lett *736*, 135247. 10.1016/j.neulet.2020.135247.

55. Belmaati Cherkaoui, M., Vacca, O., Izabelle, C., Boulay, A.-C., Boulogne, C., Gillet, C., Barnier, J.-V., Rendon, A., Cohen-Salmon, M., and Vaillend, C. (2021). Dp71 contribution to the molecular scaffold anchoring aquaporine-4 channels in brain macroglial cells. Glia *69*, 954–970. 10.1002/glia.23941.

56. Fujimoto, T., Stam, K., Yaoi, T., Nakano, K., Arai, T., Okamura, T., and Itoh, K. (2023). Dystrophin Short Product, Dp71, Interacts with AQP4 and Kir4.1 Channels in the Mouse Cerebellar Glial Cells in Contrast to Dp427 at Inhibitory Postsynapses in the Purkinje Neurons. Mol Neurobiol. 10.1007/s12035-023-03296-w.

57. Leyva-Leyva, M., Sandoval, A., Morales-Lázaro, S.L., Corzo-López, A., Felix, R., and González-Ramírez, R. (2023). Identification of Dp140 and α1-syntrophin as novel molecular interactors of the neuronal CaV2.1 channel. Pflugers Arch *475*, 595–606. 10.1007/s00424-023-02803-1.

58. Bourdon, A., François, V., Zhang, L., Lafoux, A., Fraysse, B., Toumaniantz, G., Larcher, T., Girard, T., Ledevin, M., Lebreton, C., et al. (2022). Evaluation of the dystrophin carboxy-terminal domain for micro-dystrophin gene therapy in cardiac and skeletal muscles in the DMDmdx rat model. Gene Ther *29*, 520–535. 10.1038/s41434-022-00317-6.